UNIVERSITY OF CALIFORNIA

Ernest O. Lawrence

Radiation

Laboratory

CHARGE-EXCHANGE SCATTERING OF NEGATIVE PIONS BY HYDROGEN AT 230, 260, 290, 317, and 371 MEV

BERKELEY, CALIFORNIA

UNIVERSITY OF CALIFORNIA

Lawrence Radiation Laboratory
Berkeley, California

Contract No. W-7405-eng-48

CHARGE-EXCHANGE SCATTERING OF NEGATIVE PIONS
BY HYDROGEN AT 230, 260, 290, 317, AND 371 MEV

John C. Caris

(Thesis)

March 18, 1960

CHARGE-EXCHANGE SCATTERING OF NEGATIVE PIONS
BY HYDROGEN AT 230, 260, 290, 317, AND 371 MEV

Contents

CHARGE-EXCHANGE SCATTERING OF NEGATIVE PIONS BY HYDROGEN AT 230, 260, 290, 317, AND 371 MEV

John C. Caris

Lawrence Radiation Laboratory
University of California
Berkeley, California

March 18, 1960

ABSTRACT

The differential cross section for charge-exchange scattering of negative pions by hydrogen has been observed at 230, 260, 290, 317, and 371 Mev. The reaction was observed by detecting one gamma ray from the π^0 decay with a scintillation-counter telescope. A least-squares analysis was performed to fit the observations to the function

$$\frac{d\sigma}{d\omega} = \sum_{\ell=1}^{5} a_\ell P_{\ell-1} (\cos \theta)$$

in the c.m. frame. The best fit to our experimental measurements requires only s- and p-wave scattering. The results (in mb) are:

	a_1	a_2	a_3
230 ± 9 Mev	2.50 ± 0.10	1.39 ± 0.15	2.73 ± 0.28
260 ± 7	2.02 ± 0.08	1.75 ± 0.14	2.15 ± 0.22
290 ± 9	1.45 ± 0.06	1.80 ± 0.10	1.89 ± 0.18
317 ± 8	1.40 ± 0.06	1.85 ± 0.10	1.50 ± 0.17
371 ± 9	1.08 ± 0.05	1.63 ± 0.08	1.18 ± 0.12

The least-squares analysis indicates that d-wave scattering is not established in this energy range.

I. INTRODUCTION

We measured the differential cross section for charge-exchange scattering of negative pions on hydrogen at 230, 260, 290, 317, and 371 Mev, using a scintillation-counter telescope sensitive to gamma rays from the reaction

$$\pi^- + p \rightarrow \pi^0 + n \rightarrow n + 2\gamma. \tag{1}$$

The reaction was measured by detecting one gamma ray from the decay of the π^0 meson. We performed the experiment at Berkeley in the meson cave of the 184-in. synchro-cyclotron. The energy dependence of the gamma-ray counter efficiency was measured in a separate experiment. The π^0 angular distributions were obtained from the observed gamma-ray distributions by an analysis performed by using the IBM 650 computer.

The purposes of our measurements were:
(a) to investigate the π^0 angular distributions at energies at which no data existed or, where more were desirable;
(b) to design and execute the work so as to attain greater accuracy than previously reported in our energy range;
(c) to pay special attention in the analysis to the search for d-wave scattering which has not been observed for charge-exchange scattering; and
(d) to make our work useful for future phase-shift analyses.

A brief survey of existing charge-exchange results is appropriate. When our work began no angular distributions for charge-exchange scattering were known from 220 to about 500 Mev except the counter work of Korenchenko and Zinov[1] at 307 and 333 Mev. The 220-Mev measurement was performed by Ashkin et al.[11] Recently we have learned of additional differential cross sections by Korenchenko and Zinov at 240 and 270 Mev.[2] Earlier angular distributions measured below 220 Mev[3-11] have recently been augmented by work at Chicago by Garwin et al. at 128 Mev[12] and by Kerman et al. at 61, 95, and 150 Mev[13] using a lead glass

Cherenkov detector for gamma rays. All other measurements were made with gamma-ray-sensitive scintillation-counter telescopes.

All reported work below 330 Mev has been analyzed in terms of s- and p-wave scattering only. No evidence was found suggesting the need to include d-wave scattering. The size of experimental errors, due largely to poor determination of the counter efficiency, precluded any conclusion concerning d-wave scattering at 307 and 333 Mev.[1]

Literature survey revealed three possible improvements we could make to reduce the size of errors in existing experiments and to increase the probability of detecting d-wave scattering. The specific objectives guiding the design and execution of our work embodied these improvements.

The charge-exchange differential cross section cannot be observed directly, since the π^0 meson decays isotropically in its own rest frame in a time interval somewhat less than 10^{-16} sec. One must deduce the π^0 angular distribution from a gamma-ray angular distribution observed in the laboratory system. This laboratory photon distribution is aberrated in direction and Doppler shifted in frequency by the motion of the decaying π^0 meson. We measured the reaction by detecting a single decay gamma ray from the π^0 meson.

Two kinematic characteristics of the reaction deserve mention. First, it is impossible to detect with our counter more than one decay photon from a given π^0 decay. The minimum separation angle between two photons from a decaying π^0 meson is

$$\theta_{min} = 2 \sin^{-1} \left[\frac{135}{T_\pi 0 + 135} \right], \tag{2}$$

where $T_\pi 0$ is the π^0 meson kinetic energy in Mev. Minimum separation angle, for a given $T_\pi 0$, occurs when decay photons emerge in the π^0 rest frame perpendicular to the π^0 direction of motion. Minimum separation angle occurs for π^0 mesons produced at 0 deg, i.e., those with greatest $T_\pi 0$. For 371-Mev π^0 mesons θ_{min} = 15.5 deg. Our counter subtends an angle of 11.8 deg.

Secondly, one observes at each laboratory angle a broad spectrum of photon energies. The photon angular distribution only approximates the

π^0 angular distribution in both energy and direction. Figure 1 shows
that it is kinematically possible to observe at any laboratory angle a
decay photon from a π^0 meson emitted at any angle. Thus, the net
gamma-ray counting rate at a given observation angle represents the
counter's integration over the spectrum of photon energies observable
at that angle such that each photon energy is properly weighted by

      (a) the detection efficiency for each photon energy, and

      (b) the appropriate differential cross section for the pro-

             duction of photons with each energy in a given direction.

These kinematic characteristics are background for the following dis-
cussion.

Three possible improvements in the experimental method for
charge-exchange work using scintillation-counter telescopes were
evident from a literature survey. Improvements were mandatory before
any conclusion concerning d-wave scattering was possible.

First, no experiment had measured the gamma-ray angular
distribution more forward than 20 deg (lab) except Korenchenko and
Zinov[1] at 15 deg (lab). D-wave scattering has a significant effect on
forward and backward peaking as well as a smaller peaking effect at
90 deg (c.m.) We demonstrated that 0-deg measurements were possible
provided the incident pion beam, which traversed the counter, did not
jam the anticoincidence counter.

Secondly, only two experiments had explicitly considered
energy variation of the gamma-ray detection efficiency.[4,7] Such con-
sideration is essential to treat analytically the gamma-ray spectrum
observed at each laboratory-system angle. Most reported work used
an average counter-efficiency number for each laboratory angle. These
numbers were partly measured and partly estimated.[5-10] To analyze
the net gamma-ray counting rates, explicitly considering energy variation
of the counter efficiency and analytically treating the gamma-ray spectrum
observed at each lab angle, we generalized, to include provision for
d-wave scattering, the analysis method reported by Anderson and Glicks-
man.[7] The method's details are discussed in Sec. V and Appendix A.

Thirdly, the largest single source of error in reported work
is due to detector-efficiency indeterminacy. These errors are charac-
teristically 10% to 15%. Ashkin et al.[11] report 5% indeterminacy at
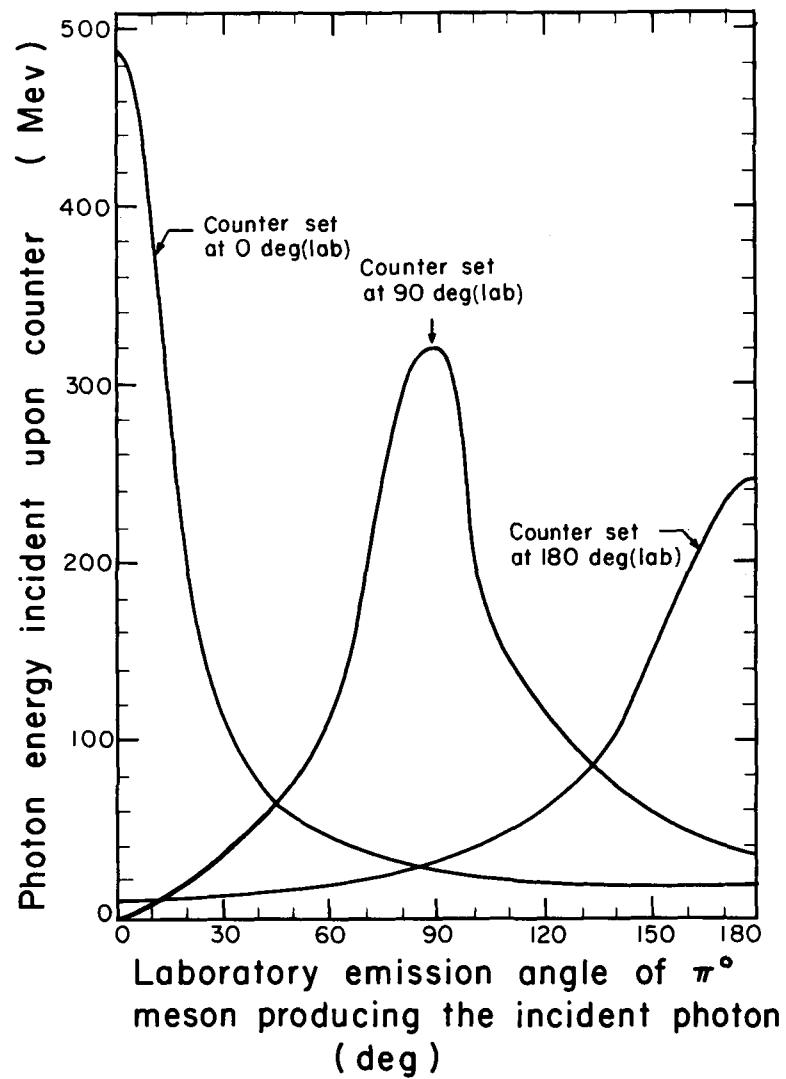
Fig. 1. Kinematics of the charge-exchange reaction showing, for a
given counter setting, the energy of a decay photon incident upon
the counter as a function of the emission angle (lab) of the π^0
meson producing the photon. (Plotted for 371-Mev incident π^-.)

220 Mev. Most reported work neglects counter-efficiency variation for photons incident upon the counter face off center and off normal. We found by measurement that such variation is not negligible for our geometry (Sec. VI. F). We developed the counter calibration method discussed in Sec. VI for two reasons:

> (a) to measure the detector's explicit energy dependence necessary for the analysis method mentioned above, and
>
> (b) to reduce efficiency indeterminacy to less than 10%.

The three preceding paragraphs summarize the general ideas that guided the design and execution of our experiment.

II. EXPERIMENTAL ARRANGEMENT

A. Magnet System

Our experimental arrangement for the 260-, 317-, and 371-Mev measurements is shown in Figs. 2 and 3.

Negative pions created on an internal beryllium target by the impinging 730-Mev proton beam were partially momentum-analyzed by the cyclotron fringe field. We used an 8-in.-bore doublet quadrupole magnet between the cyclotron vacuum tank and the 8-ft-diameter iron collimator.

Final momentum analysis and bending through 55 deg was performed by a wedge focusing magnet. We designed the pole tips, beam entrance angle, and beam exit angle to give equal horizontal and vertical focusing. The 8-in.-bore symmetrical triplet quadrupole adjusted the beam focus on the liquid hydrogen target.

We used a 2-ft-thick lead brick shield for the counter area. The 3-in.-diameter collimator was cast in a 4X4X24-in. lead brick. We inserted telescoping brass tubes in the 3-in. diameter tube to provide the 1-3/4-in.-diameter collimator used at all energies.

We performed measurements at 230 and 290 Mev during a second experimental run. The arrangement was modified to use available magnets. Two smaller magnets, each bending the beam approximately 30 deg, replaced the wedge focusing magnet. We substituted a 4-in.-bore triplet quadrupole for the 8-in.-bore quadrupole. Otherwise, the experimental arrangement was identical for both runs. A slightly larger energy spread was observed at 230 and 290 Mev owing to the magnet substitutions.
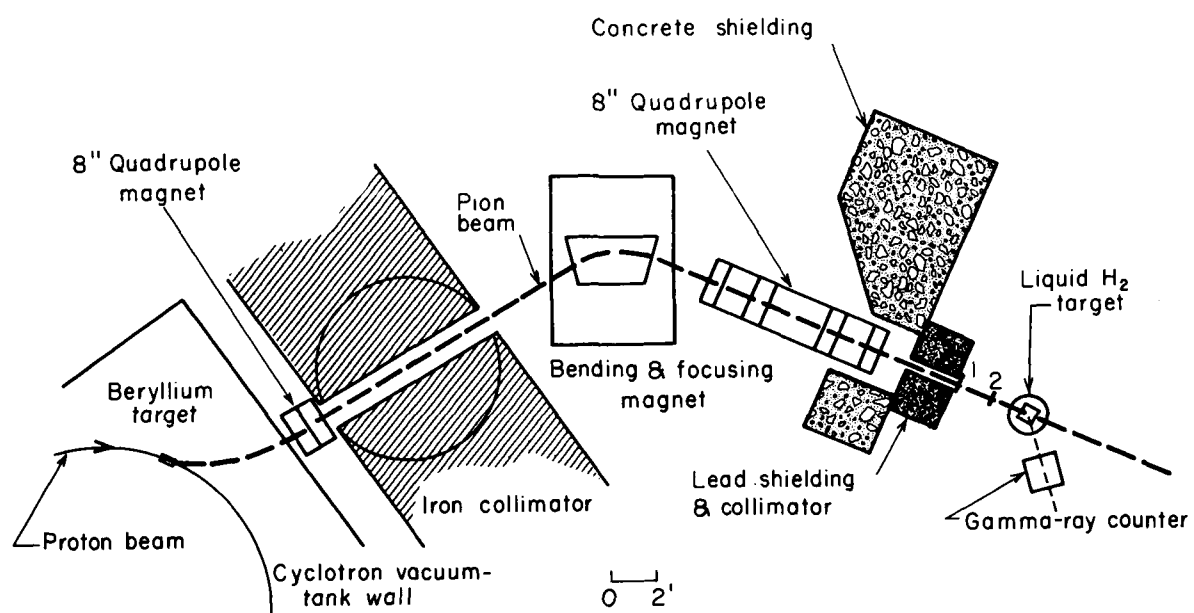
Fig. 2. Diagram of the experimental arrangement.
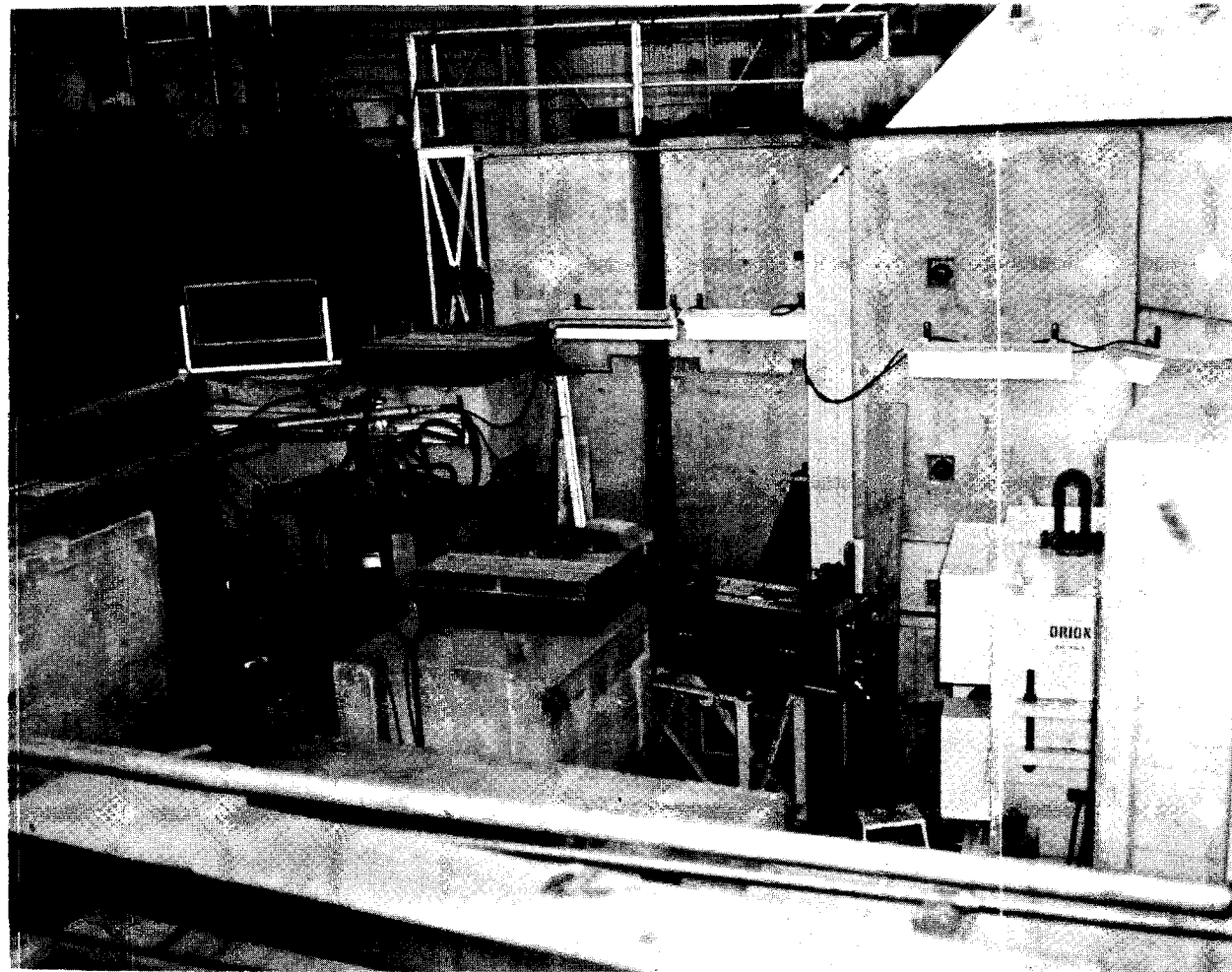
ZN-2155

Fig. 3. Experimental arrangement in the meson cave, showing the
Orion wedge magnet, the 8-in.-bore quadrupole magnet, and the
liquid hydrogen target.

B. Pion Beams

Table I summarizes the pion beam characteristics.

Table I

Negative-pion-beam characteristics			
Energy (Mev)	ΔT (Mev)	% Muons	% Electrons
230	± 8	10 ± 1.0	4.7 ± 1.0 [a]
260	± 7	10 ± 1.0	3 ± 2 [b]
290	± 9	7.4 ± 0.8	1.0 ± 0.5 [a]
317	± 8	6.0 ± 1.0	2 ± 1 [b]
371	± 9	4.0 ± 1.0	2 ± 1 [b]

[a] Electron contamination measured with gas Cherenkov counter.

[b] Electron contamination estimated by calculation.

We determined magnet fields by wire-orbit measurements. Final energies, energy spreads, and muon contaminations were obtained by range-curve analysis. Figure 4 shows the integral and differential range curves for 371 Mev. The range curve segment between points A and B is the region where pions are stopping.

We defined the beam energy as corresponding to the midpoint of segment AB. The energy spread was defined by

(a) considering the full energy spread to extend from the 10% to 90% points of AB, and

(b) correcting this estimate to include pion range straggling in copper.

Table I includes a 1.5-Mev subtraction for incident-pion energy loss in the first one-half of the hydrogen target.

Point B determines muon contamination from

(a) pions decaying before the last bending magnet, and

(b) those pions decaying after the bending magnet which produce muons with ranges greater than 230 g/cm^2 Cu.
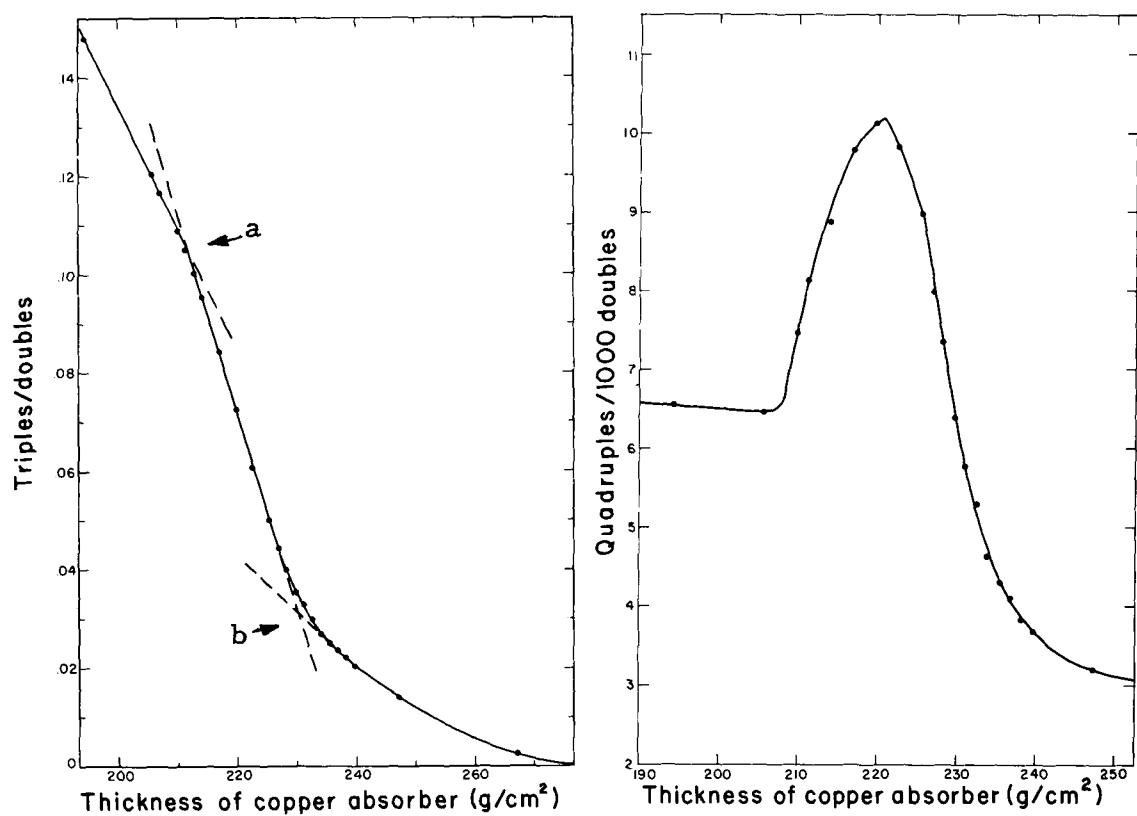
Fig. 4. Integral and differential range curves for the 371-Mev π^--meson beam.

The muon contamination was corrected in two ways. We showed by calculation that muon-beam contamination with ranges less than 230 g/cm^2 Cu was 1±0.5% for all energies. Secondly, we calculated muon losses due to multiple Coulomb scattering in the thick copper absorber. This correction was negligible for our beams.

Electron contamination was measured for the 230- and 290-Mev beams by using a gas Cherenkov counter as the central unit in a three-counter telescope. We used sulfur hexafluoride gas at 40 and 80 psi pressure. No such counter was available during the run at 260, 317, and 371 Mev. Our electron-contamination estimates by calculation agree well with those measured.

Figure 5 shows horizontal and vertical pion beam profiles at the hydrogen target. We measured profiles with a 1-in.-diameter counter in coincidence with the beam monitor counters. Profile width due to 1-in. counter resolution is subtracted from Fig. 5.

C. Electronics

Figure 6 shows the electronics block diagram. Evans coincidence units[14] and Hewlett-Packard type 460A distributed amplifiers were used throughout. Our scalers were driven by Perez-Mendez – Swift amplitude discriminators.[15] They have an adjustable threshold from 0.1 to 1.5 volts and are rated at 10^7 pulses per second instantaneous rate. We used a Hewlett-Packard type 520A prescaler, rated at 10^7 pps, in the beam monitor circuit and Model II decade scalers,[14] rated at 10^6 pps, for final scaling throughout.

Photomultiplier tube bases for monitor counters 1 and 2 were modified for high instantaneous counting rates by placing a 1-μf capacitor at the last stage. Dynode voltage decreased less than 1% during beam fallout pulses.

Each coincidence circuit was pulser tested for 5×10^6 pps instantaneous rate. The pulser output duplicated the cyclotron rate, 64 pulse groups per sec, each of 400 μsec duration. Instantaneous counting rates for these tests exceeded rates used during the experiment.
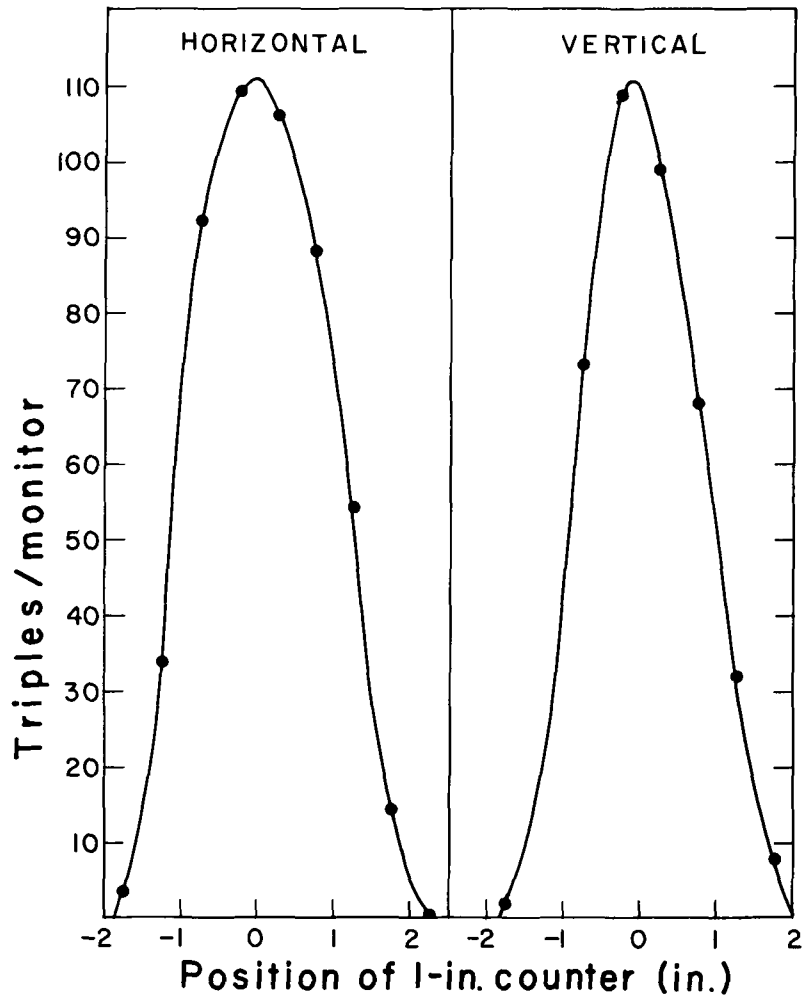
MU—17542

Fig. 5. Horizontal and vertical beam profiles measured at the position of the liquid hydrogen target.
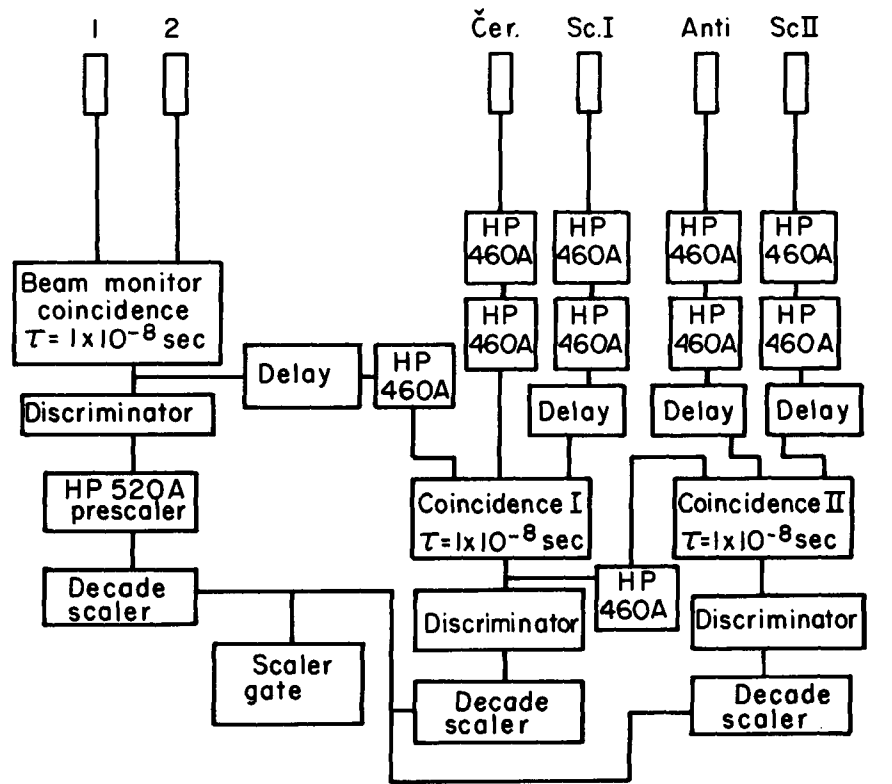
Fig. 6. Electronics block diagram.

A gamma ray was inferred by the conditions:

(a) a monitor coincidence between 1 and 2;

(b) a Coincidence I from simultaneous monitor coincidence, Cherenkov pulse, and Sc. I pulse; and

(c) a Coincidence II from simultaneous Coincidence I pulse, Sc II pulse, and no simultaneous anticoincidence pulse.

D. Counter Telescope

We measured the charge-exchange reaction by detecting single decay gamma rays from the π^0 mesons. Counter details and the hydrogen target arrangement are shown in Figs. 7 and 8.

A familiar type of scintillation-counter telescope was used (Fig. 9). It contains a removable Pb converter 1/4 in. thick and a lucite Cherenkov counter which eliminates accidental counts due to slow charged particles. Figure 10 shows a lead curve observed while counting gamma rays from the charge-exchange reaction.
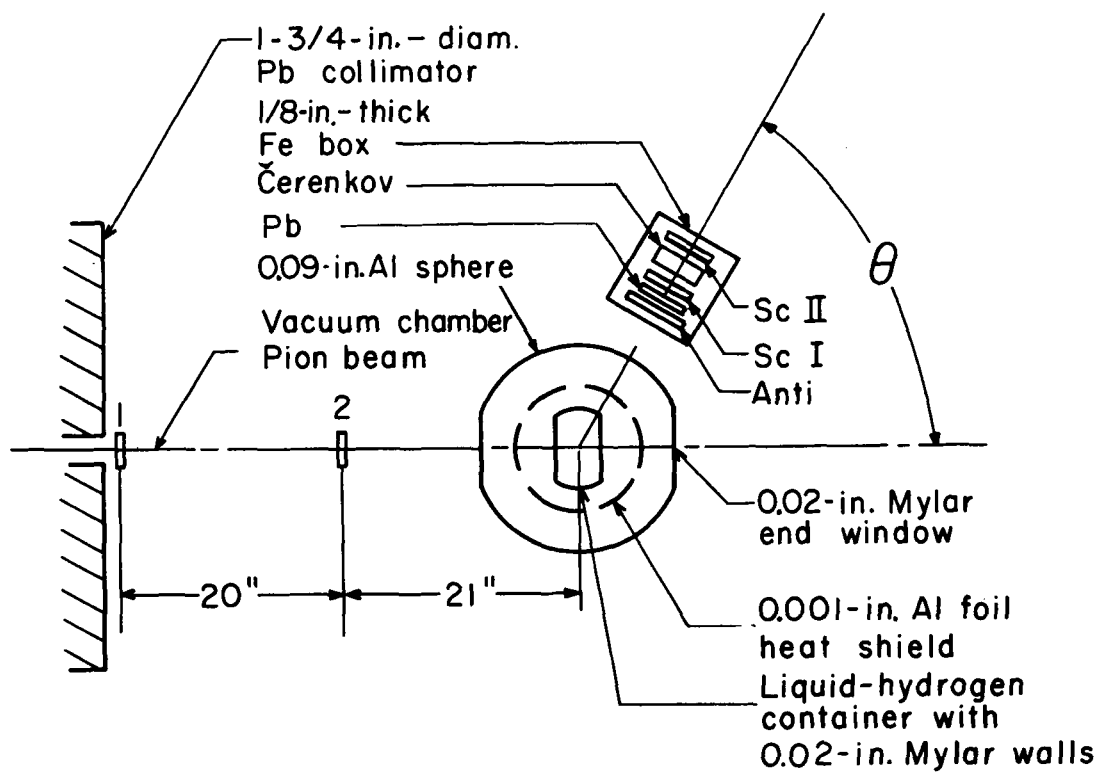
Sc. I, Sc. II, and the anti-coincidence counter are composed of a solid solution of para-terphenyl in polystyrene and are viewed by RCA 6199 photomultiplier tubes through lucite light pipes. Two RCA 6810 photomultiplier tubes, with signals added, view the Cherenkov counter.

We magnetically shielded the photomultiplier tubes two ways. Each phototube was first surrounded by two concentric shields. The inner shield was 1/32-in.-thick μ metal and the outer shield was 1/4-in.-thick soft iron. Rubber O rings provided spacing between shields. Secondly, the telescope was mounted within a 1/8-in.-thick soft iron box.

A small beta-active source attached to each scintillator provided a means for daily checks on the detection sensitivity of each coincidence channel.

The lead converter defined the counter's subtended solid angle. Edge effects due to gamma rays striking the converter near the edges or at an angle from the normal are not negligible. We corrected for these effects by experimental measurements (Sec. VII).

Beam-monitor scintillator 1 was 3X3X1/4 in., scintillator 2 was 2-in. in diameter by 1/4 in. thick. They were viewed by RCA 6810A photomultiplier tubes. Their composition was para-terphenyl in polystyrene.

1-3/4-in.- diam.
Pb collimator

1/8-in.-thick
Fe box

Čerenkov

Pb

0.09-in. Al sphere

Vacuum chamber

Pion beam

Sc II
Sc I
Anti

θ

0.02-in. Mylar
end window

0.001-in. Al foil
heat shield

Liquid-hydrogen
container with
0.02-in. Mylar walls

2

20"

21"

MU—19804

Fig. 7. Liquid hydrogen target and counter telescope diagram.
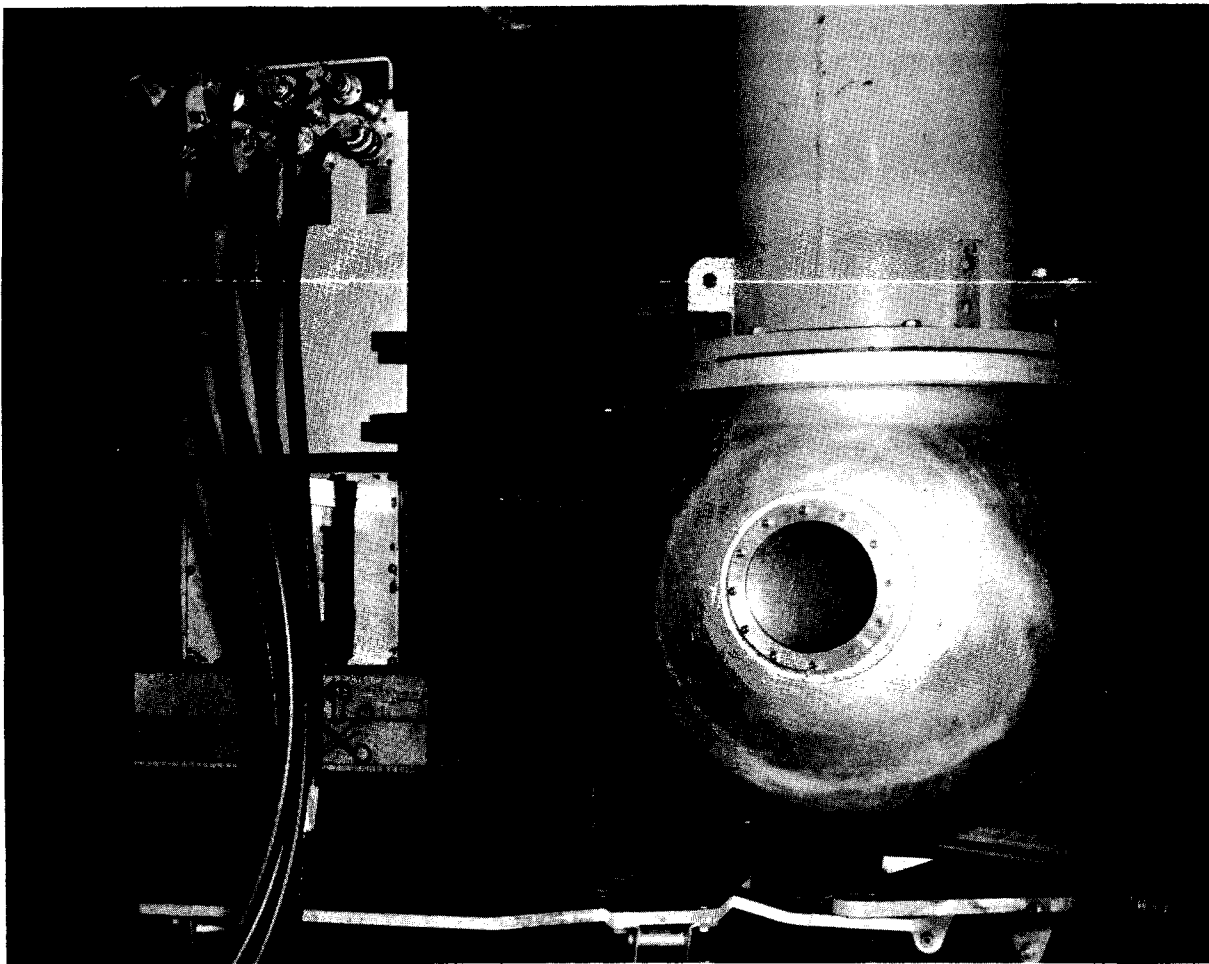
ZN-2396

Fig. 8. Gamma-ray counter telescope and liquid hydrogen target
    arrangement.
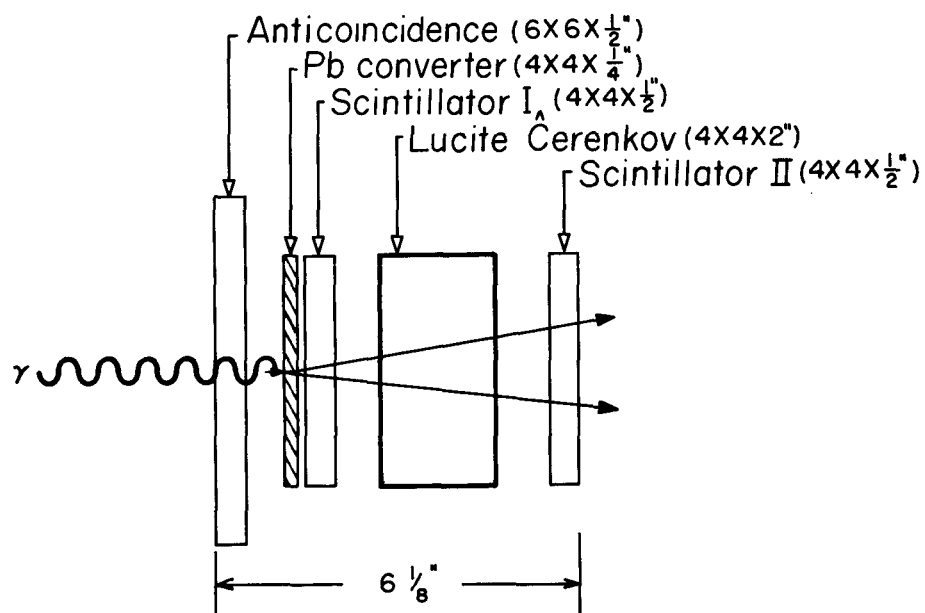
Fig. 9. Gamma-ray counter telescope schematic.
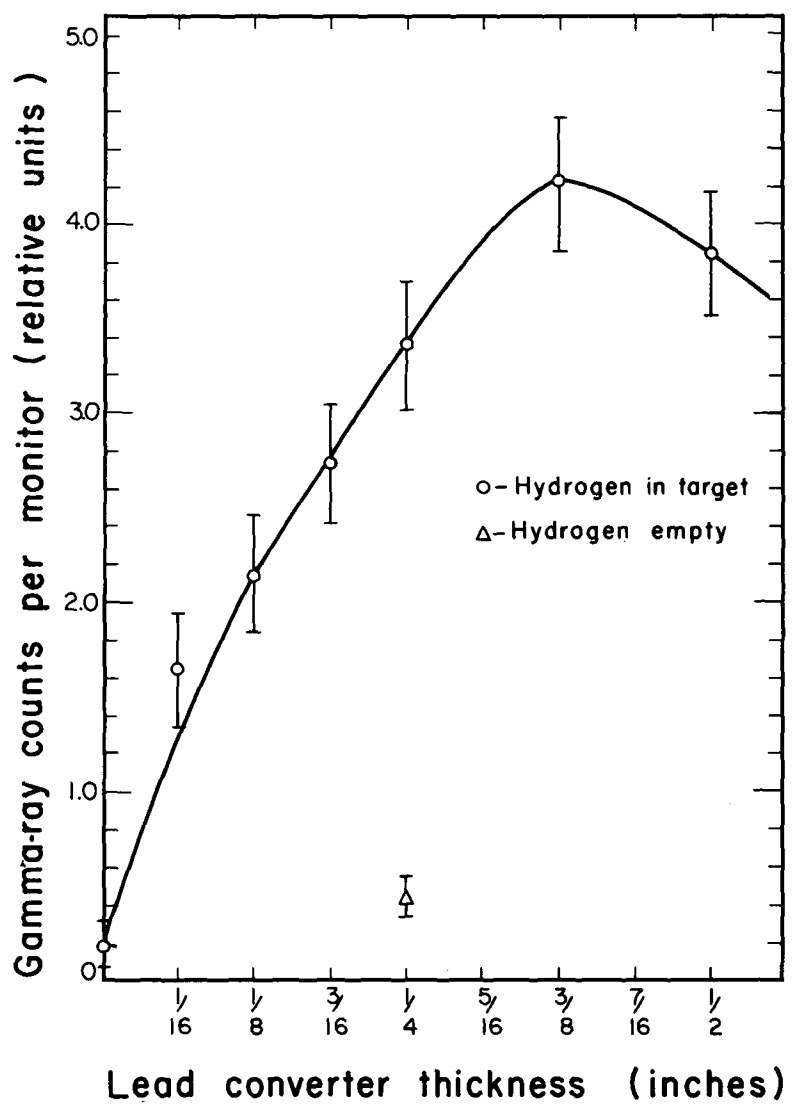
Fig. 10. Gamma-ray telescope counting rate as a function of
Pb converter thickness. The lead-in to lead-out ratio is 17 to 1
for a 1/4-in. lead converter. The target-full to target-empty
ratio is 8 to 1 for a 1/4-in. lead converter. This curve observed
at 40 deg (lab).

All counters exhibited broad, flat plateaus. No long-term drift of the counter-telescope efficiency was detected.

E. Liquid Hydrogen Target

The hydrogen target reservoir has been previously described.[16] The spherical vacuum jacket was formed by welding together two spun aluminum hemispheres. The jacket was 0.090 in. thick. Beam entry and exit windows were laminated Mylar sheet 0.020 in. thick and 4.5 in. in diameter. An aluminum flange clamped the end windows in place. Vacuum seal was made by an O ring between the Mylar sheet and the flange base.

Hydrogen-cell walls were 0.020-in.-thick laminated Mylar sheet. The walls were bonded by a Versamid-epoxy resin to 1/4-in.-thick brass plates forming the top and bottom. Cell dimensions were 5 in. high, 4 in. thick, and 8 in. long with 2-in. end radii. A 0.001-in. aluminum foil heat shield, with beam entry and exit holes, surrounded the hydrogen cell. The cell's condition was visually checked through the end windows. The hydrogen cell was emptied by:

(a) closing the target cell vent line by a solenoid valve, and

(b) introducing H_2 gas pressure (5 psi) into the vent line.

A grid of dots placed on the cell faces served two purposes:

(a) target alignment, and

(b) target thickness measurements.

Beam-profile measurements defined the beam's trajectory in space. The target was aligned by adjustment screws so that the beam axis traversed the hydrogen cell's center. An internal pressure of 1 atmosphere bows the hydrogen cell walls. The grid enabled us to measure the bow accurately.

III. EXPERIMENTAL TECHNIQUE

Observation angles ranged from 0 to 155 deg (lab). We measured the gamma-ray angular distributions for at least nine laboratory-system angles. Running-time limitations determined this number. Net gamma-ray counting rates per incident negative pion resulted from series of eight individual measurements at each lab angle. Eight measurements were necessary to include all combinations of target full and empty, Pb converter in and out and, "accidental" cables in and out. Net counting rate is given by

$$
\left(\frac{\gamma}{M}\right)_{Net} = \left[\left(\frac{\gamma}{M}\right)_{H_2, Pb} - \left(\frac{\gamma}{M}\right)_{H_2, No Pb}\right] - \left[\left(\frac{\gamma}{M}\right)_{No H_2, Pb} - \left(\frac{\gamma}{M}\right)_{No H_2, No Pb}\right]
$$

$$
- \left[\left(\frac{\gamma}{M}\right)_{H_2, Pb} - \left(\frac{\gamma}{M}\right)_{H_2, No Pb}\right]_{accidental} + \left[\left(\frac{\gamma}{M}\right)_{No H_2, Pb} - \left(\frac{\gamma}{M}\right)_{No H_2, No Pb}\right]_{accidental} \tag{3}
$$

We measured accidental counts by delaying the monitor coincidence circuit output by one fine-structure bunch time (5.4×10^{-8} sec) relative to the gamma-ray counter. Accidental measurements are discussed fully in Sec. VII. We made measurements of net counting rate at each angle as part of a regular cycle. At least three cycles were completed for each incident pion energy. No net counting rate was found statistically at variance with those of different cycles. Table II shows typical counting rates for 260-Mev incident negative pions.

We took special precautions at 0 and 10 deg. At 0 deg the incident pion beam traversed the counter and was electronically rejected by the anticoincidence counter. We made careful jamming checks for various incident pion fluxes. Forward data were found independent of beam flux below 8000 incident pions per sec on a time-average basis. Fluxes from 13,000 to 17,000 incident pions per sec (time average) were used for angles of 20 deg or greater.

Table II

Observed gamma-ray counts per million incident pions at 260 ± 7 Mev.

Target and converter condition	Type of Measurement	Angle (lab) (deg)								
		0	10	20	28.7	40	60	83.2	110	155.7
H_2 in	Real	173.25±1.46	137.54±1.88	96.44±1.01	75.79±1.20	51.80±0.71	25.79±0.54	11.94±0.33	9.51±0.27	11.12±0.34
Pb in	Accidental	9.17±0.97	2.50±0.79	3.40±0.58	2.86±0.52	2.80±0.53	1.47±0.38	0.88±0.33	0.43±0.25	0.72±0.16
H_2 in	Real	7.60±0.78	12.15±0.78	7.72±0.56	4.34±0.42	2.35±0.34	1.57±0.23	0.90±0.21	0.95±0.22	0.63±0.18
Pb out	Accidental	0.50±0.50	0.86±0.50	0.60±0.35	0.16±0.16	0.20±0.20	0.20±0.20	0.40±0.28	0	0
H_2 out	Real	83.13±1.47	55.08±1.77	17.20±0.65	7.76±0.34	6.06±0.42	3.00±0.31	1.88±0.22	1.80±0.18	2.60±0.22
Pb in	Accidental	7.75±1.40	2.15±0.57	1.14±0.40	0.83±0.21	1.00±0.38	0.60±0.35	0	0.45±0.20	0.86±0.20
H_2 out	Real	5.40±0.70	9.76±0.88	4.09±0.42	0.50±0.17	0.15±0.09	0	0.27±0.13	0.47±0.18	0.40±0.16
Pb out	Accidental	0	0.60±0.35	0	0	0	0	0.20±0.14	0.17±0.17	0
Net counting rates		87.00±2.92	79.98±3.07	73.95±1.95	62.32±1.44	41.95±1.13	20.55±0.86	8.76±0.66	7.08±0.56	8.43±0.54

Our measurements were made during two separate cyclotron experiments. Measurements at 260, 317, and 371 Mev were made simultaneously with our colleague Perkins,[17] who studied the reaction

$$\pi^- + p \rightarrow \pi^- + n + \pi^+ . \tag{4}$$

The experiment of 230 and 290 Mev was performed simultaneously with our colleague Goodwin, who studied the elastic scattering

$$\pi^- + p \rightarrow \pi^- + p . \tag{5}$$

We measured the π^--proton total attenuation cross section at 230 and 290 Mev in an experiment that will be reported elsewhere.

Miscellaneous experimental details are:

(a) all photomultiplier signals were at least 4 volts at the coincidence circuit inputs,

(b) the detection sensitivity of coincidence channels was maintained constant by daily source count checks and slight photomultiplier tube voltage adjustments based thereon, and

(c) discriminator tripping levels were maintained uniform at 2 volts input photomultiplier pulse by daily pulser checks.

IV. DATA ANALYSIS

Most reported experiments analyze the observed gamma-ray angular distributions by using

$$\frac{d\sigma_\gamma}{d\omega} = \frac{(\gamma/M)_{net}}{ntfG\Delta\Omega\bar{\epsilon}} \tag{6}$$

where $(\gamma/M)_{net}$ is the net gamma-ray counting rate per incident pion, nt is the target thickness in protons/cm^2, f is the pion percentage of the beam, $G\Delta\Omega$ is the corrected solid angle in sterad (see Sec. VII), and $\bar{\epsilon}$ is the detector efficiency for the average gamma-ray energy observed at a given angle. The gamma-ray differential cross section is fitted to the function

$$\frac{d\sigma_\gamma}{d\omega} = \sum_\ell b_\ell P_{\ell-1}(\alpha) \tag{7}$$

It is convenient for the least-squares analysis to designate the coefficients as a_1 through a_5. For this reason we express the differential cross section in the form above rather than in the form $\dfrac{d\sigma}{d\omega} = \sum_{\ell=0}^{4} a_\ell P_\ell(\cos\theta)$.

The charge-exchange differential cross section is then obtained in the form

$$\frac{d\sigma_\pi^0}{d\omega} = \sum_\ell a_\ell P_{\ell-1}(\alpha) \tag{8}$$

by use of the fact that each a_ℓ is directly proportional to the corresponding b_ℓ.[5]

This treatment is not quite correct, however. The detector efficiency for the average-energy gamma ray used in Eq. (6) is not a good approximation to the average detection efficiency at a given angle, since we know the incident gamma rays range widely in energy and the detector efficiency varies rapidly with energy. Korenchenko and Zinov adopted this approximate treatment for their experiments at 240, 270,

307, and 333 Mev. [1,2] The above introduction makes clear the need for a more exact analysis method if one is striving for the maximum obtainable accuracy.

We refer the reader to Appendix 1 for a complete derivation of the analysis method used for our experiment. This method avoids approximation at the expense of greater complexity. To exhibit the method's ideas we will present a brief outline of the relations derived in Appendix 1.

Beginning with Eq. (8), expressing the charge-exchange cross section in terms of the desired coefficients, a_ℓ, one derives the gamma-ray differential cross section in the laboratory frame,

$$\frac{d\sigma_\gamma}{d\Omega} = \frac{1}{(\gamma_0 - n_0 z)^2} \sum_{\ell=1}^{5} a_\ell P_{\ell-1}(y) \int_{-1}^{+1} \frac{P_{\ell-1}(x)dx}{(\gamma-nx)^2} , \qquad (9)$$

where the symbols used are defined by Table XXII and Fig. 35 of Appendix 1 and the equation is numbered as in Appendix 1. The integral of (9) expresses the analytical form for the gamma-ray spectrum observed at a given angle. The gamma-ray differential cross section is related to the observed counting rates by defining an "apparent" cross section for gamma-ray production in the center-of-mass system, [7]

$$\frac{d\sigma_\gamma}{d\Omega} = \frac{(\gamma/M)_{net} (\gamma_\theta - n_\theta z)^2}{ntfG\,\Delta\Omega} . \qquad (10)$$

Equating (9) and (10) we have

$$\frac{(\gamma/M_{net}(\gamma_0 - n_0 z)^2}{ntfG\Delta\Omega} = \sum_{\ell=1}^{5} a_\ell P_{\ell-1}(y) \int_{-1}^{+1} \frac{\epsilon(x,z)P_{\ell-1}(x)dx}{(\gamma-nx)^2} , \qquad (11)$$

where the detector efficiency $\epsilon(x,z)$ has been placed under the integral sign. The quantity $G\Delta\Omega$ depends slightly on x and should ideally be included in the integrand of (11). Neglecting this dependence formally is a very good approximation because (a) the dependence is slight and (b) suitable averages have been made for the quantity $G\Delta\Omega$ (Sec. VII. B).

The analysis treatment is exact except for this approximation.

To express (11) in convenient form for least-squares solution for the coefficients, a_ℓ, we define

$$Y(z) = \frac{(\gamma/M)_{net}(\gamma_0 - n_0 z)^2}{ntfG\Delta\Omega}$$

$$\overline{\epsilon_\ell(z)} = \frac{1}{K_\ell} \int_{-1}^{+1} \frac{\epsilon(x, z)P_{\ell-1}(x)}{(\gamma - nx)^2} dx \qquad (12)$$

$$K_\ell = \int_{-1}^{+1} \frac{P_{\ell-1}(x)}{(\gamma - nx)^2} dx.$$

Finally we obtain a set of linear equations

$$Y(z) = \sum_{\ell=1}^{5} a_\ell X_\ell(z), \qquad (13)$$

where

$$X_\ell(z) = P_{\ell-1}(y) \, \overline{\epsilon}_\ell(z) \, K_\ell \qquad (14)$$

and

$$y = \left(\frac{\gamma_0 z - n_0}{\gamma_0 - n_0 z} \right). \qquad (15)$$

There are as many equations in the set (13) as there are laboratory-system observing angles.

The integrals $\overline{\epsilon}_\ell(z) \, K_\ell$ are integrable in closed form. Numerical evaluation of the expressions for $\overline{\epsilon}_\ell(z)$, K_ℓ, $P_{\ell-1}(y)$, and $X_\ell(z)$ was performed using the IBM 650 computer.

We now define the least-squares problem and outline its solution. The least-squares problem is to solve sets of equations (13) for the coefficients a_ℓ. We have either nine or ten such equations in each set. A special characteristic of our problem is that the quantities $X_\ell(z)$ are not members of a complete orthonormal set of functions.

Therefore, we derived a general least-squares solution and programmed it for IBM 650 computation. We applied the general least-squares theory of Deming[18] to our problem.

This program, named LSMFT, performs a least-squares solution of (13) for coefficients a_ℓ, considering as many as 10 variables $Y(z)$, 50 variables $X_\ell(z)$ and 5 parameters a_ℓ. Fewer variables and coefficients may be used at the programmer's discretion. The variables $X_\ell(z)$ need not have any particular functional properties. The program first obtains a trial solution for the coefficients, a_ℓ, by solving five or fewer of the equations (13) by a matrix-inversion subroutine. The program then uses the trial solution to obtain final values for the a_ℓ by minimizing the least-squares sum of weighted residuals. At the programmer's discretion the program automatically iterates the solution any number of times. In practice we found, as expected from Deming's theory, that iteration more than once does not improve the solution.

Input data required for the LSMFT program are the experimental values of $Y(z)$, $X_\ell(z)$, their weights defined by

$$W_{Y(z)} = \frac{1}{(\Delta Y(z))^2} \, , \tag{16}$$

$$W_{X_{\ell(z)}} = \frac{1}{(\Delta X_\ell(z))^2} \, ,$$

the number of equations in the set, and the number of parameters, a_ℓ, to be used in the fit. The errors, $\Delta Y(z)$ and $\Delta X_\ell(z)$, were computed by propagating, through the expressions for $\Delta Y(z)$ and $\Delta x_\ell(z)$, the errors assigned to their individual factors.

The computer output for LSMFT includes the trial solutions for a_ℓ; the final least-squares solutions for a_ℓ; the reciprocal, or error, matrix; the least-squares sum; and information useful for checking the program's internal operation.

V. RESULTS

We present the results in two parts: (**A**) results of the experimental observations, and (B) results of the least-squares analyses based on the observations.

A. Experimental Results

Figures 11 through 15 show the observed gamma-ray angular distributions. To indicate the relative sizes of the various counting rates combined by Eq. (3) to give the net gamma-ray counting rates we presented Table II (See Sec. III). This table gives the observed counting rates for 260-Mev incident pions. Relative counting rates are typical of those for other incident pion energies. Tables III through VII present the corrected experimental results used for the least-squares analysis. (In Sec. VII there is a detailed discussion of the corrections applied to the observed counting rates and the experimental geometry.)

B. Analysis Results

We recall that the least-squares analysis by LSMFT program performs a fit of the experimental observations to the function

$$\frac{d\sigma}{d\omega} = \sum_{\ell-1}^{5} a_\ell P_{\ell-1}(\alpha) . \tag{8}$$

The analysis results in the coefficients, a_ℓ; their errors, δa_ℓ; and statistical criteria for the goodness of a given fit. To obtain evidence pertinent to the presence of d-wave scattering in the charge-exchange reaction we performed least-squares analyses assuming that only s-wave scattering is present, assuming that only s- and p-wave scattering are present, and then assuming that s-, p-, and d-wave scattering are present. Tables VIII through XII present the results of these least-squares analyses. The reported errors in the coefficients were computed from the error matrices given in Tables XIII through XVII by the relation

$$(\delta a_\ell)^2 = c_{\ell\ell}\sigma^2 = c_{\ell\ell}, \tag{17}$$

where $c_{\ell\ell}$ is a diagonal element of the error matrix and σ is the variance of a function of unit weight.
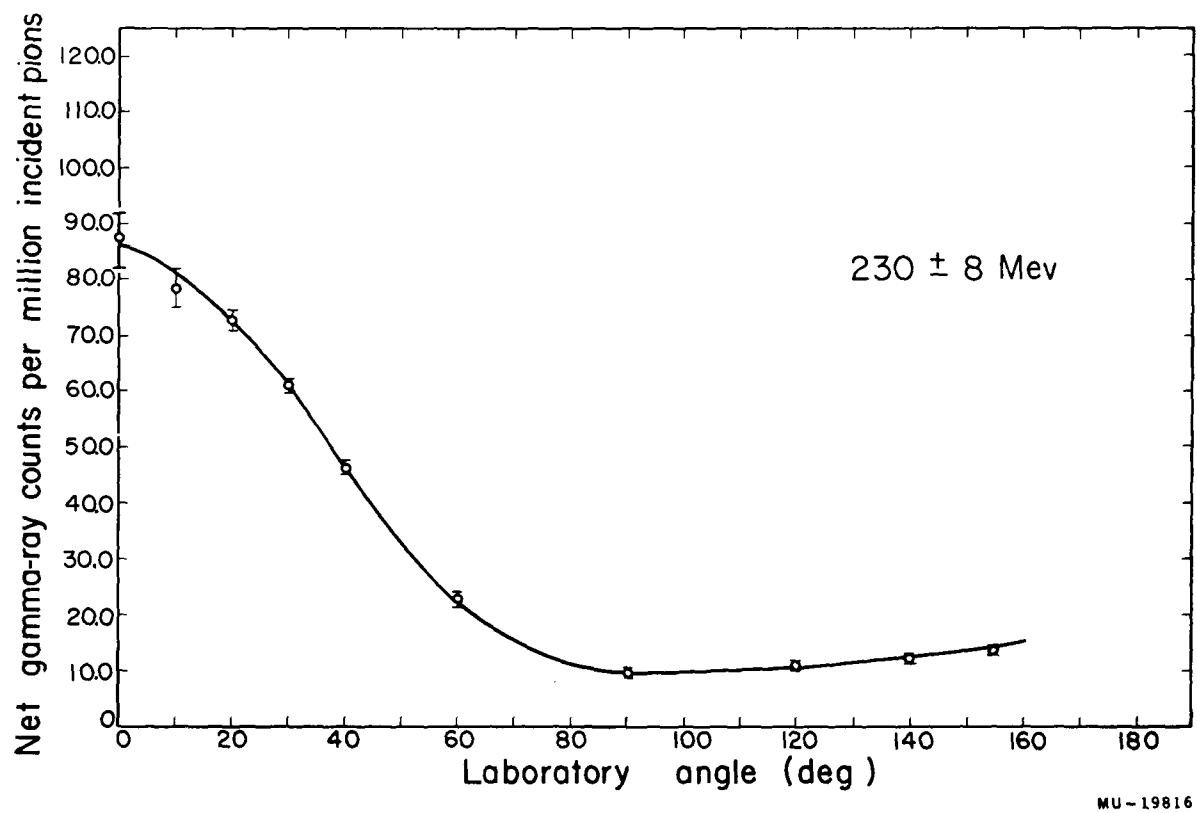
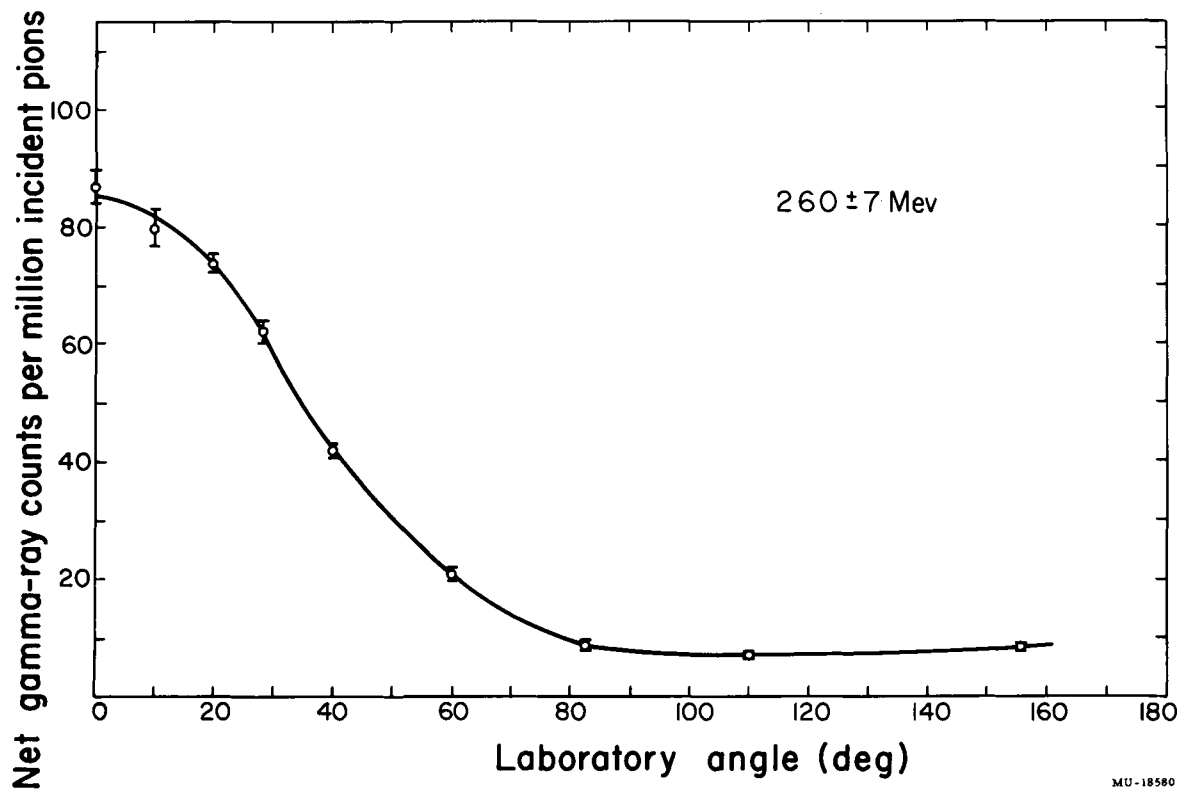Fig. 11. Observed gamma-ray angular distribution at 230 Mev.

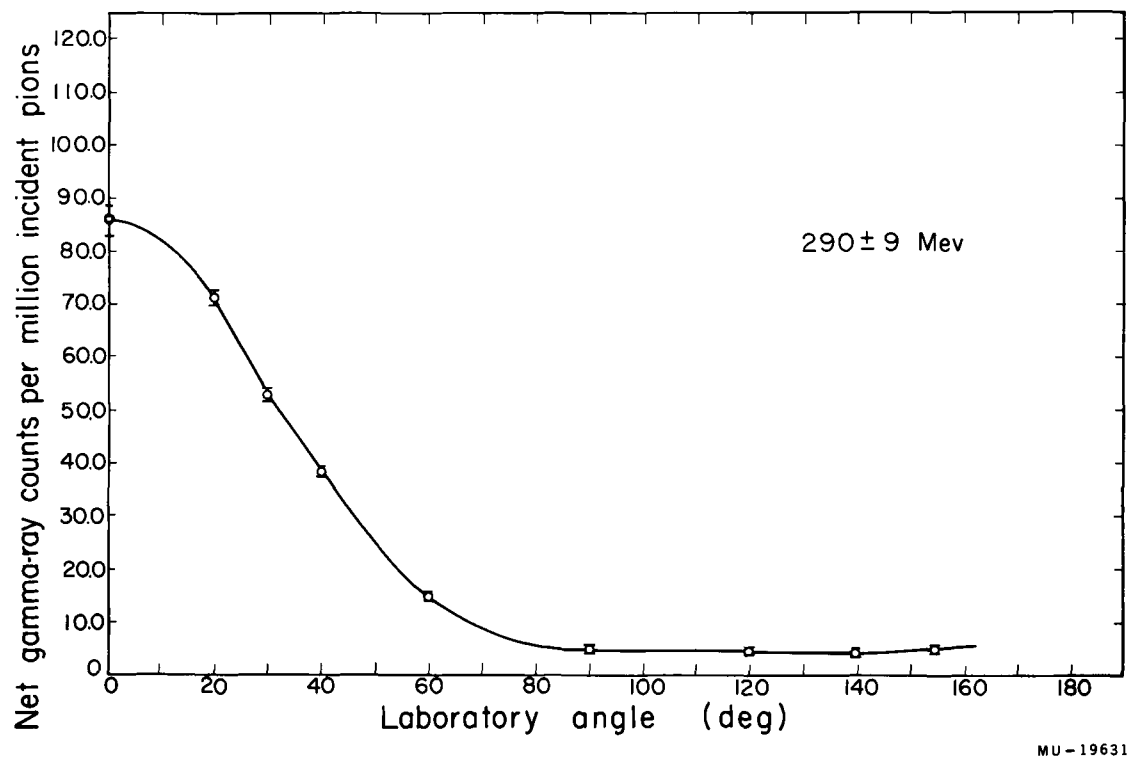Fig. 12. Observed gamma-ray angular distribution at 260 Mev.

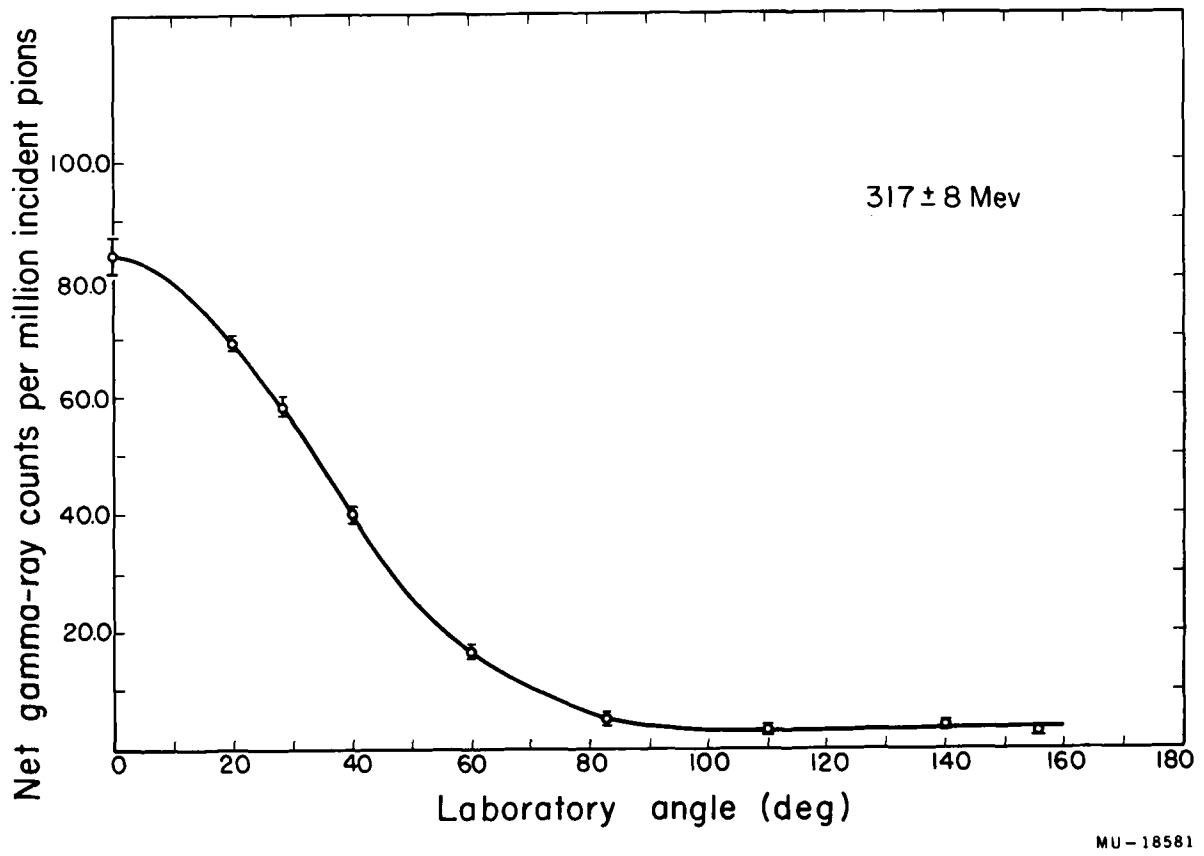**Fig. 13.** Observed gamma-ray angular distribution at 290 Mev.

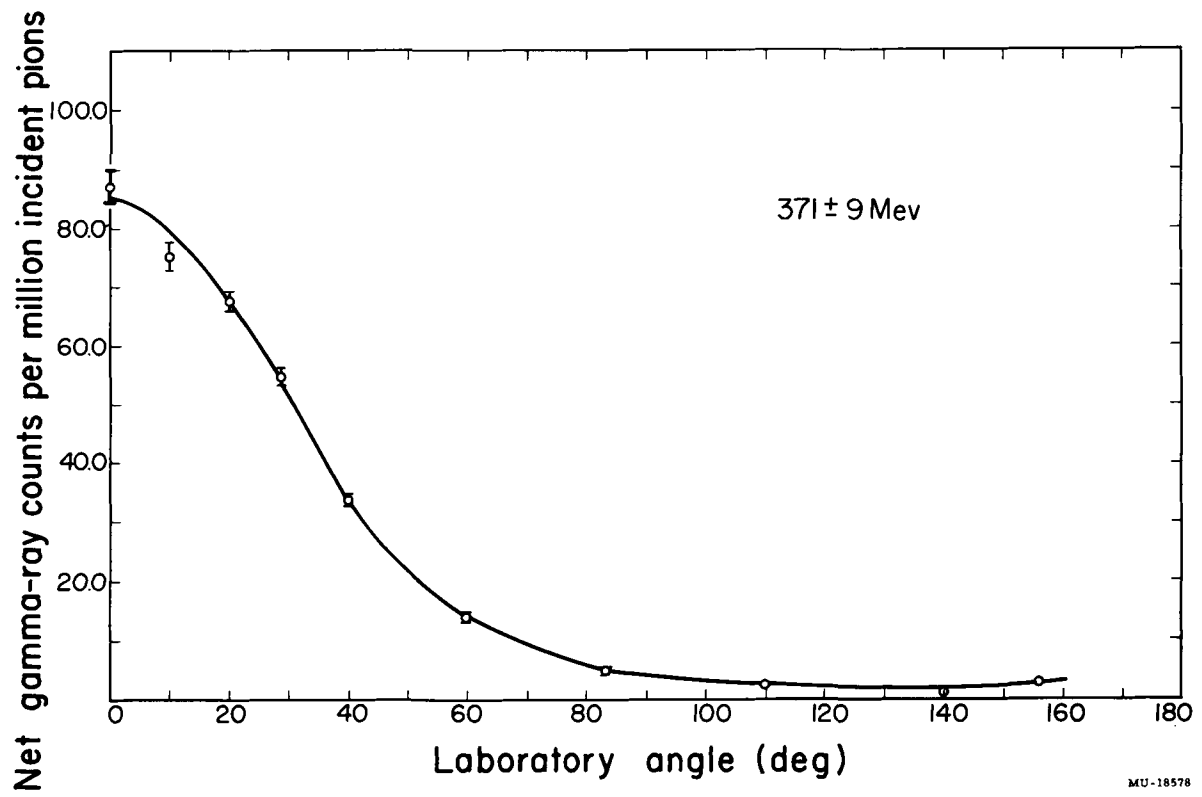Fig. 14. Observed gamma-ray angular distribution at 317 Mev.

Fig. 15. Observed gamma-ray angular distribution at 371 Mev.

Table III

	Net count rate		
Angle (lab) (deg)	Observed (corrected for accidentals only) (counts $\times 10^{-6}$)	Final corrected $(\gamma/M)_{net}$ (counts $\times 10^{-6}$)	$G\Delta\Omega$ (steradian)
0	87.19 ± 2.45	88.24 ± 2.49	0.03700± .00037
10	78.20 ± 3.18	79.12 ± 3.21	0.03695± .00037
20	72.44 ± 1.21	73.28 ± 1.27	0.03673± .00037
30	61.17 ± 1.22	61.85 ± 1.26	0.03638± .00036
40	46.30 ± 0.96	46.77 ± 0.99	0.03599± .00036
60	22.94 ± 0.84	23.09 ± 0.85	0.03514± .00035
90	9.98 ± 0.55	9.97 ± 0.55	0.03458± .00035
120	11.04 ± 0.56	11.07 ± 0.56	0.03515± .00035
140	12.04 ± 0.53	12.09 ± 0.54	0.03599± .00036
155	13.92 ± 0.72	14.00 ± 0.73	0.03647± .00036

The table caption reads: Experimental results for 230-Mev incident π^- mesons

γ = 2.138 ± 0.038

η = 1.890 ± 0.044

γ_0 = 1.036 ± 0.002

η_0 = 0.2711± 0.0062

$\overline{nt}$ = (4.56 ± .09)$\times 10^{23}$ protons/cm^2

f = 85.3% ± 1.4%

Table IV

	Experimental results for 260-Mev incident π^- mesons		
	Net count rate		
Angle (lab) (deg)	Observed (corrected for accidentals only) (counts $\times 10^{-6}$)	Final corrected $(\gamma/M)_{net}$ (counts $\times 10^{-6}$)	$G\Delta\Omega$ (steradian)
0	87.00 ± 2.92	87.97 ± 2.95	0.03702 ± .00037
10	79.98 ± 3.07	80.87 ± 3.09	0.03695 ± .00037
20	73.95 ± 1.59	74.75 ± 1.64	0.03673 ± .00037
28.7	62.32 ± 1.44	62.97 ± 1.48	0.03644 ± .00036
40	41.95 ± 1.13	42.32 ± 1.15	0.03599 ± .00036
60	20.55 ± 0.86	20.65 ± 0.87	0.03514 ± .00035
83.2	8.76 ± 0.66	8.73 ± 0.66	0.03455 ± .00034
110	7.08 ± 0.56	7.05 ± 0.56	0.03480 ± .00035
155.7	8.43 ± 0.54	8.44 ± 0.54	0.03660 ± .00037

γ = 2.264 ± 0.029

η = 2.031 ± 0.032

γ_0 = 1.038 ± 0.001

η_0 = 0.2891 ± 0.0047

$\overline{nt}$ = (4.56 ± .09) $\times 10^{23}$ protons/cm^2

f = 87.0% ± 2.2%

Table V

	Net count rate		
Angle (lab) (deg)	Observed (corrected for accidentals only) (counts $\times 10^{-6}$)	Final corrected $(\gamma/M)_{net}$ (counts $\times 10^{-6}$)	$G \Delta\Omega$ (steradian)
0	86.26 ± 2.34	86.93 ± 2.49	0.03702 ± .00037
20	71.21 ± 1.35	71.69 ± 1.41	0.03673 ± .00037
30	52.77 ± 1.19	53.03 ± 1.24	0.03638 ± .00036
40	38.38 ± 1.06	38.49 ± 1.09	0.03599 ± .00036
60	14.47 ± 0.69	14.31 ± 0.70	0.03514 ± .00035
90	4.73 ± 0.50	4.55 ± 0.51	0.03458 ± .00035
120	4.53 ± 0.43	4.40 ± 0.43	0.03515 ± .00035
140	4.03 ± 0.37	3.91 ± 0.37	0.03599 ± .00036
155	5.00 ± 0.66	4.91 ± 0.66	0.03647 ± .00036

Experimental results for 290-Mev incident π^- mesons

γ = 2.385 ± 0.036

η = 2.166 ± 0.039

γ_0 = 1.047 ± 0.002

η_0 = 0.3111 ± 0.0058

$\bar{\eta}t$ = (4.56 ± .09) $\times 10^{23}$ protons/cm^2

f = 91.6% ± 1.3%

Table VI

	Net count rate		
Angle (lab) (deg)	Observed (corrected for accidentals only) (counts $\times 10^{-6}$)	Final corrected $(\gamma/M)_{net}$ (counts $\times 10^{-6}$)	$G \Delta \Omega$ (steradian)
0	84.31 ± 3.01	84.64 ± 3.06	0.03702 ± .00037
20	69.41 ± 1.31	69.58 ± 1.37	0.03673 ± .00037
28.7	58.42 ± 1.51	58.48 ± 1.57	0.03644 ± .00036
40	40.14 ± 0.88	40.01 ± 0.95	0.03599 ± .00036
60	16.69 ± 0.63	16.39 ± 0.67	0.03514 ± .00035
83.2	5.08 ± 0.59	4.76 ± 0.62	0.03455 ± .00035
110	3.05 ± 0.44	2.80 ± 0.45	0.03480 ± .00035
140	4.06 ± 0.32	3.87 ± 0.34	0.03600 ± .00036
155.7	3.17 ± 0.42	3.00 ± 0.43	0.03660 ± .00037

Experimental results for 317-Mev incident π^- mesons

$\gamma = 2.492 \pm 0.031$

$\eta = 2.283 \pm 0.034$

$\gamma_0 = 1.049 \pm 0.002$

$\eta_0 = 0.3255 \pm 0.0050$

$\overline{n}t = (4.56 \pm .09) \times 10^{23}$ protons/cm^2

$f = 92.0\% \pm 2.2\%$

Table VII

Experimental results for 371-Mev incident π^- mesons

Angle (lab) (deg)	Net count rate		$G \Delta \Omega$ (steradian)
	Observed (corrected for accidentals only) (counts $\times 10^{-6}$)	Final corrected $(\gamma/M)_{net}$ (counts $\times 10^{-6}$)	
0	87.38 ± 2.86	86.10 ± 2.99	0.03702 ± .00037
10	75.23 ± 2.36	73.83 ± 2.49	0.03696 ± .00037
20	67.63 ± 1.47	66.24 ± 1.66	0.03673 ± .00037
28.7	54.91 ± 1.01	53.51 ± 1.20	0.03644 ± .00036
40	33.73 ± 0.73	32.28 ± 0.90	0.03599 ± .00036
60	14.03 ± 0.56	12.75 ± 0.69	0.03514 ± .00035
83.2	4.91 ± 0.43	3.92 ± 0.52	0.03455 ± .00035
110	2.65 ± 0.45	1.93 ± 0.50	0.03480 ± .00035
140	1.34 ± 0.35	0.72 ± 0.40	0.03600 ± .00036
155.7	2.90 ± 0.33	2.39 ± 0.39	0.03660 ± .00037

$\gamma = 2.699 \pm 0.033$

$\eta = 2.507 \pm 0.036$

$\gamma_0 = 1.060 \pm 0.002$

$\eta_0 = 0.3578 \pm 0.050$

$\overline{n}t = (4.56 \pm .09) \times 10^{23}$ protons/cm^2

$f = 94.0\% \pm 1.5\%$

Table VIII

Results of rhe least-squares fits of the 230 ± 8-Mev measurements to the function $\frac{d\sigma}{d\Omega} = \sum_{\ell} a_{\ell} P_{\ell}(q)$ for different values of ℓ (the number of coefficients used for the fit) and k (the number of degrees of freedom)

	$\ell=1, k=8$	$\ell=2, k=7$	$\ell=3, k=6$	$\ell=4, k=5$	$\ell=5, k=4$
a_1	$3.24\pm.10$	$2.99\pm.10$	$2.50\pm.10$	$2.50\pm.10$	$2.50\pm.10$
a_2	---	$1.62\pm.16$	$1.39\pm.15$	$1.47\pm.16$	$1.47\pm.16$
a_3	---	---	$2.73\pm.28$	$2.77\pm.28$	$2.82\pm.30$
a_4	---	---	---	$0.29\pm.25$	$0.26\pm.26$
a_5	---	---	---	---	$-0.34\pm.78$

Least-squares sum S of weighted residuals

	183.7	85.35	2.41	1.09	0.89

Table IX

Results of the least-squares fits of the 260±7-Mev measurements to the function $\frac{d\sigma}{d\Omega} = \sum_{\ell} a_\ell P_{\ell-1}(\mu)$ for different values of ℓ (the number of coefficients used for the fit) and k (the number of degrees of freedom)

	$\ell=1, k=7$	$\ell=2, k=6$	$\ell=3, k=5$	$\ell=4, k=4$	$\ell=5, k=3$
a_1	2.80±0.08	2.20±0.08	2.02±0.08	2.02±0.08	2.02±0.08
a_2	---	2.18±0.14	1.75±0.14	1.76±0.15	1.75±0.15
a_3	---	---	2.15±0.22	2.16±0.22	2.20±0.24
a_4	---	---	---	0.05±0.19	0.03±0.20
a_5	---	---	---	---	-0.25±0.55
Least-squares sum S of weighted residuals	299.3	93.29	1.62	1.56	1.35

Table X

Results of the least-squares fits of the 290±9-Mev measurements to the function $\frac{d\sigma}{d\Omega} = \sum_\ell a_\ell P_\ell(\rho)$ for different values of ℓ (the number of coefficients used for the fit) and k (the number of degrees of freedom)

	$\ell=1, k=7$	$\ell=2, k=6$	$\ell=3, k=5$	$\ell=4, k=4$	$\ell=5, k=3$
a_1	1.77±0.06	1.68±0.06	1.45±0.06	1.45±0.06	1.45±0.06
a_2	---	1.81±0.11	1.80±0.10	1.77±0.11	1.77±0.11
a_3	---	---	1.89±0.18	1.89±0.18	1.91±0.19
a_4	---	---	---	-0.17±0.16	-0.18±0.16
a_5	---	---	---	---	-0.16±0.45
Least-squares sum S of weighted residuals	462.9	107.68	2.03	0.94	0.82

Table XI

Results of the least-squares fits of the 317±8-Mev measurements to the function $\frac{d\sigma}{d\Omega} = \sum_{\ell} a_\ell P_\ell(\rho)$ for different values of ℓ (the number of coefficients used for the fit) and k (the number of degrees of freedom)

	$\ell=1$, k=7	$\ell=2$, k=6	$\ell=3$, k=5	$\ell=4$, k=4	$\ell=5$, k=3
a_1	1.51±0.05	1.51±0.06	1.40±0.06	1.40±0.06	1.39±0.06
a_2	- - -	1.86±0.10	1.85±0.10	1.85±0.10	1.87±0.11
a_3	- - -	- - -	1.50±0.17	1.49±0.17	1.50±0.17
a_4	- - -	- - -	- - -	0.02±0.15	0.01±0.15
a_5	- - -	- - -	- - -	- - -	-0.35±0.42

Least-squares sum S of weighted residuals

	$\ell=1$, k=7	$\ell=2$, k=6	$\ell=3$, k=5	$\ell=4$, k=4	$\ell=5$, k=3
residuals	514.2	82.44	1.69	1.65	0.93

Table XII

Results of the least-squares fits of the 371 ± 9-Mev measurements to the function $\frac{d\sigma}{d\Omega} = \sum_{\ell} a_\ell P_\ell(q)$ for different values of ℓ(the number of coeffcients used for the fit) and k(the n umber of degrees of freedom)

	$\ell=1, k=8$	$\ell=2, k=7$	$\ell=3, k=6$	$\ell=4, k=5$	$\ell=5, k=4$
a_1	1.30 ± 0.04	1.18 ± 0.05	1.08 ± 0.05	1.08 ± 0.05	1.08 ± 0.05
a_2	- - -	1.72 ± 0.08	1.63 ± 0.08	1.62 ± 0.08	1.62 ± 0.08
a_3	- - -	- - -	1.18 ± 0.12	1.18 ± 0.12	1.16 ± 0.13
a_4	- - -	- - -	- - -	-0.07 ± 0.11	-0.06 ± 0.11
a_5	- - -	- - -	- - -	- - -	0.16 ± 0.27

Least-squares sum S of weighted residuals

	660.5	94.23	4.47	4.12	3.80

Table XIII

Error matrices for the one-coefficient fits

230-Mev	$c_{11} = 0.00930$
260-Mev	$c_{11} = 0.00625$
290-Mev	$c_{11} = 0.00332$
317-Mev	$c_{11} = 0.00268$
371-Mev	$c_{11} = 0.00192$

Table XIV. Error matrices for the two-coefficient fits

$$\begin{array}{ccc} c_{11} & c_{12} \\ & c_{22} \end{array}$$

230 Mev

.00903 - .00297

.0240

260 Mev

.00658 - .00475

.0192

290 Mev

.00380 - .000326

.0110

317 Mev

.00331 - .000034

.0104

371 Mev

.00220 - .000357

.00659

Table XV. Error matrices for the three-coefficient fits

$$
\begin{array}{ccc}
c_{11} & c_{12} & c_{13} \\
& c_{22} & c_{23} \\
& & c_{33}
\end{array}
$$

230 Mev

.00942 - .00125 -.0120
        .0214   -.00620
                .0759

260 Mev

.00615 - .00350 -.00340
        .0198   -.0101
                 .0467

290 Mev

.00384 - .000269 -.00332
        .0106   -.0000099
                  .0319

317 Mev

.00334   .0000070 -.00191
        .0103   -.00029
                    .0274

371 Mev

.00218 - .000231 -.00119
        .00647   -.00112
                  .0152

Table XVI. Error matrices for the four-coefficient fits

$$
\begin{array}{cccc}
c_{11} & c_{12} & c_{13} & c_{14} \\
 & c_{22} & c_{23} & c_{24} \\
 & & c_{33} & c_{34} \\
 & & & c_{44}
\end{array}
$$

230 Mev

.00946	-.00144	-.0121	-.000648
	-.0260	-.00409	.0167
		.0775	.00839
			.0644

260 Mev

.00618	-.00372	-.00350	-.000806
	.0221	-.00889	.00909
		.0474	.00489
			.0364

290 Mev

.00384	-.000341	-.00334	-.000431
	.0113	-.000108	.00455
		.0319	-.000644
			.0262

317 Mev

.00334	.00035	-.00192	.00020
	.0108	-.00047	.00325
		.0275	-.00127
			.0225

371 Mev

.00218	-.000192	-.00119	.000173
	.00696	-.00108	.00256
		.0152	.00012
			.0127

Table XVII. Error matrices for the five-coefficient fits

$$\begin{array}{ccccc} c_{11} & c_{12} & c_{13} & c_{14} & c_{15} \\ & c_{22} & c_{23} & c_{24} & c_{25} \\ & & c_{33} & c_{34} & c_{35} \\ & & & c_{44} & c_{45} \\ & & & & c_{55} \end{array}$$

230 Mev

.00952	-.00149	-.0130	-.000116	.00624
	.0261	-.00344	.0163	-.00420
		.0921	.000406	-.0936
			.0689	.0518
				.609

260 Mev

.00628	-.00395	-.00270	-.00118	-.00463
	.0229	-.0115	.0103	.0143
		.0571	.00051	-.0536
			.0386	.0249
				.302

290 Mev

.00385	-.000349	-.00350	-.000367	.00157
	.0113	.0000030	.00449	-.00109
		.0342	-.00151	-.00213
			.0265	.00828
				.205

317 Mev

.00335	-.000012	-.00192	.000229	.000909
	.0112	-.00031	.00294	-.00830
		.0277	-.00139	-.00359
			.0228	.00642
				.175

371 Mev

.00219	-.000164	-.00108	.000147	-.000953
	.00699	-.000857	.00250	-.00196
		.0160	-.000100	-.00789
			.0127	.00190
				.0725

For random processes, such as observed counting rates, whose frequency is distributed according to the Poisson distribution the variance of a function of unit weight is taken as unity. Section VIII discusses the least-squares analyses in detail.

The coefficients a_1, a_2, a_3, a_4 and a_5 as a function of incident pion kinetic energy are plotted on Figs. 16 through 20. Figures 16, 17, and 18 also show the experimental results of Korenchenko and Zinov.[12]

The charge-exchange angular distributions computed from the coefficients a_ℓ by Eq. (8) are shown in Fig. 21. The coefficients used are those for the three-coefficient fit, which is the "best" fit as described in Sec. VIII.

Figure 22 shows the charge-exchange total cross section as a function of incident pion kinetic energy. The total cross sections shown in Table XVIII were computed by integrating Eq. (8),

$$\sigma = 4\pi (a_1 \pm \delta a_1) \tag{18}$$

All known charge-exchange experiments are plotted on Fig. 22.
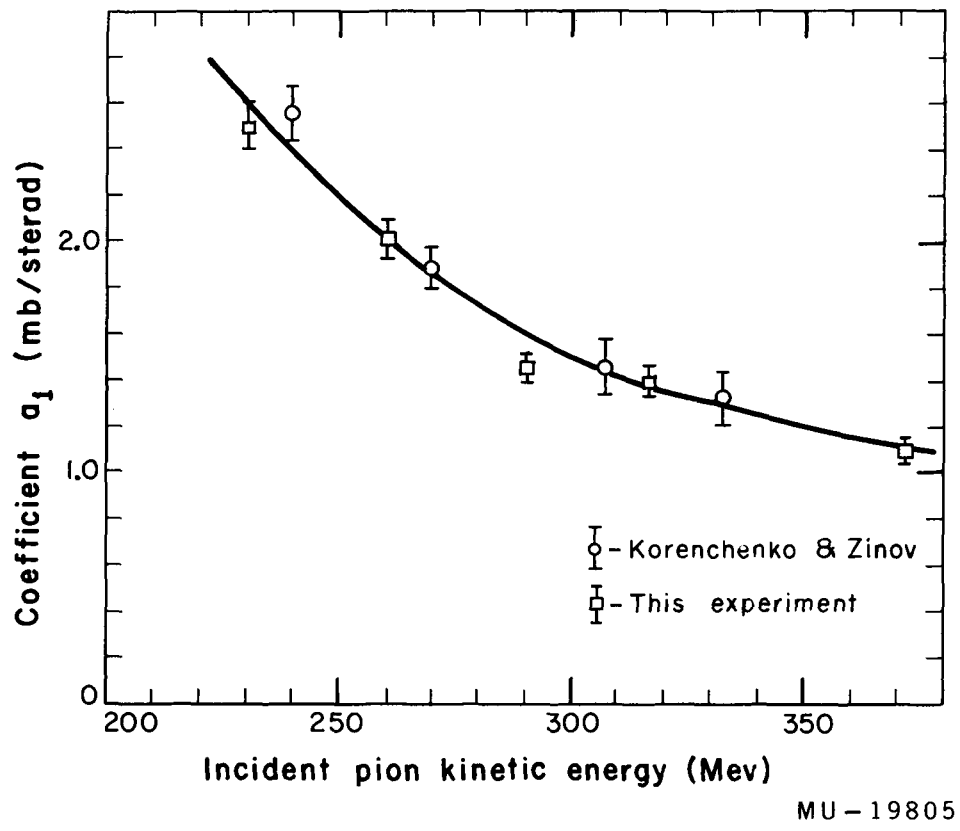
MU−19805

Fig. 16. Coefficient a_1 vs. incident pion kinetic energy.
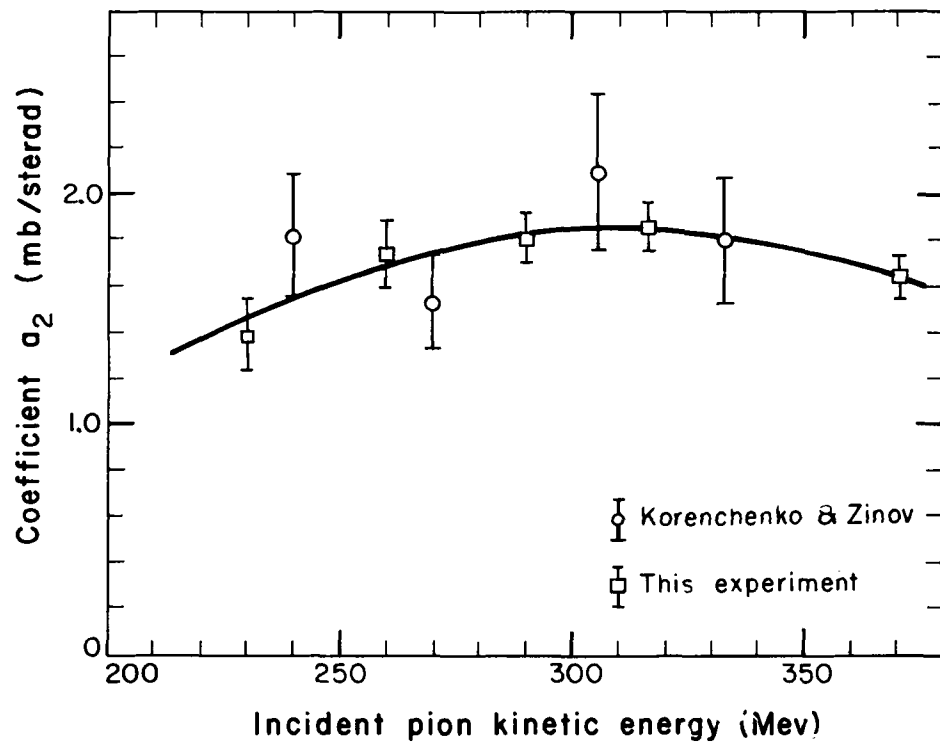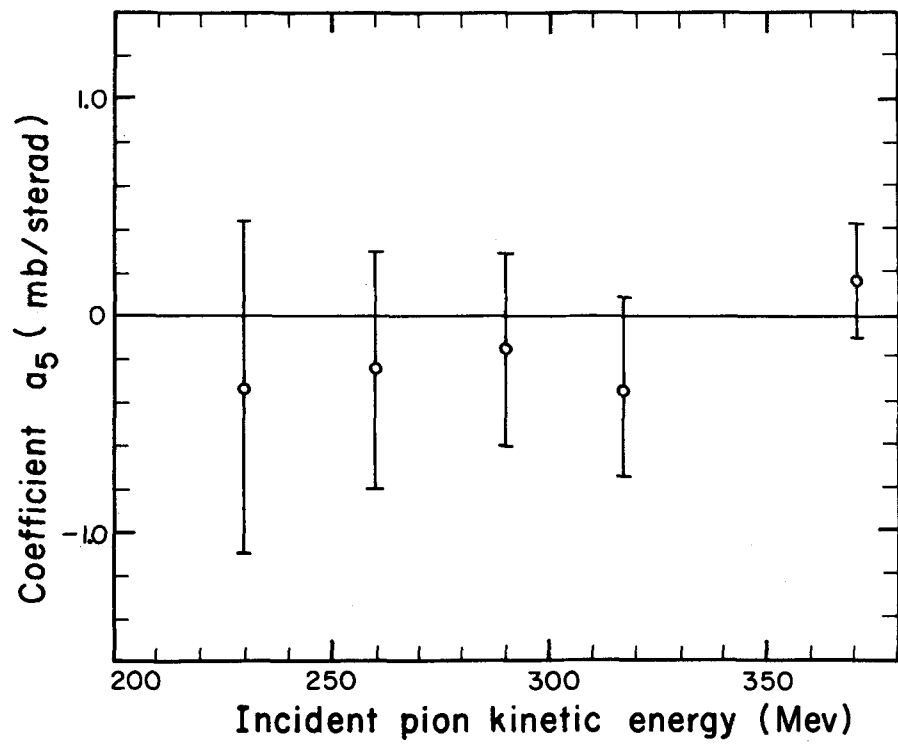
MU−19806

Fig. 17. Coefficient a_2 vs. incident pion kinetic energy.
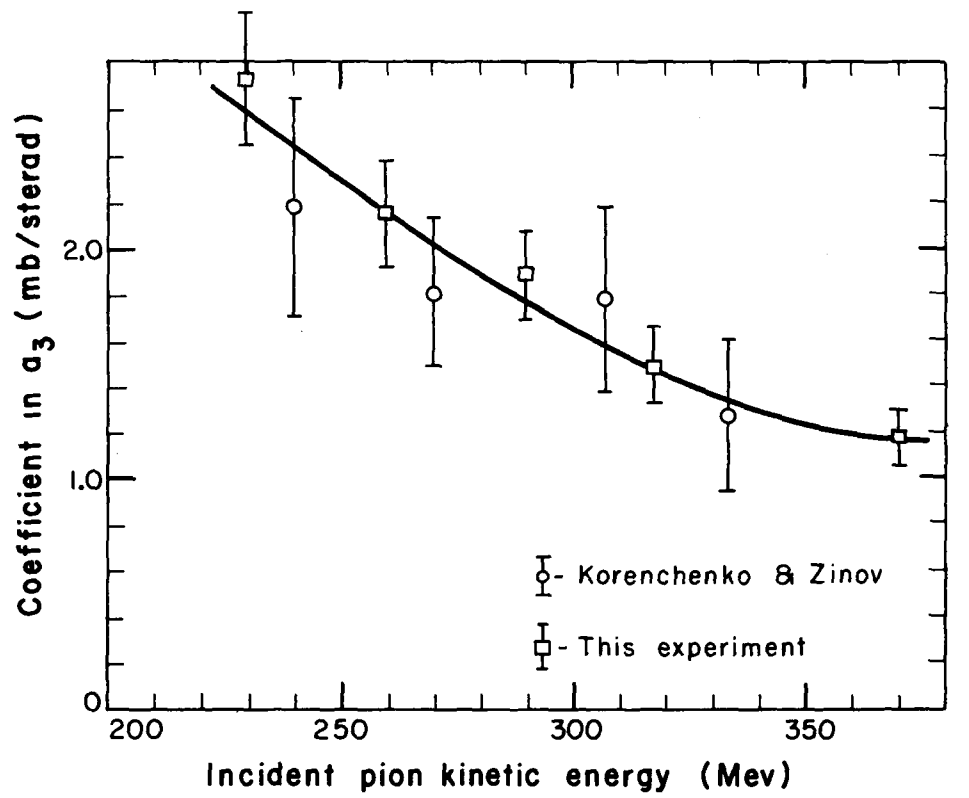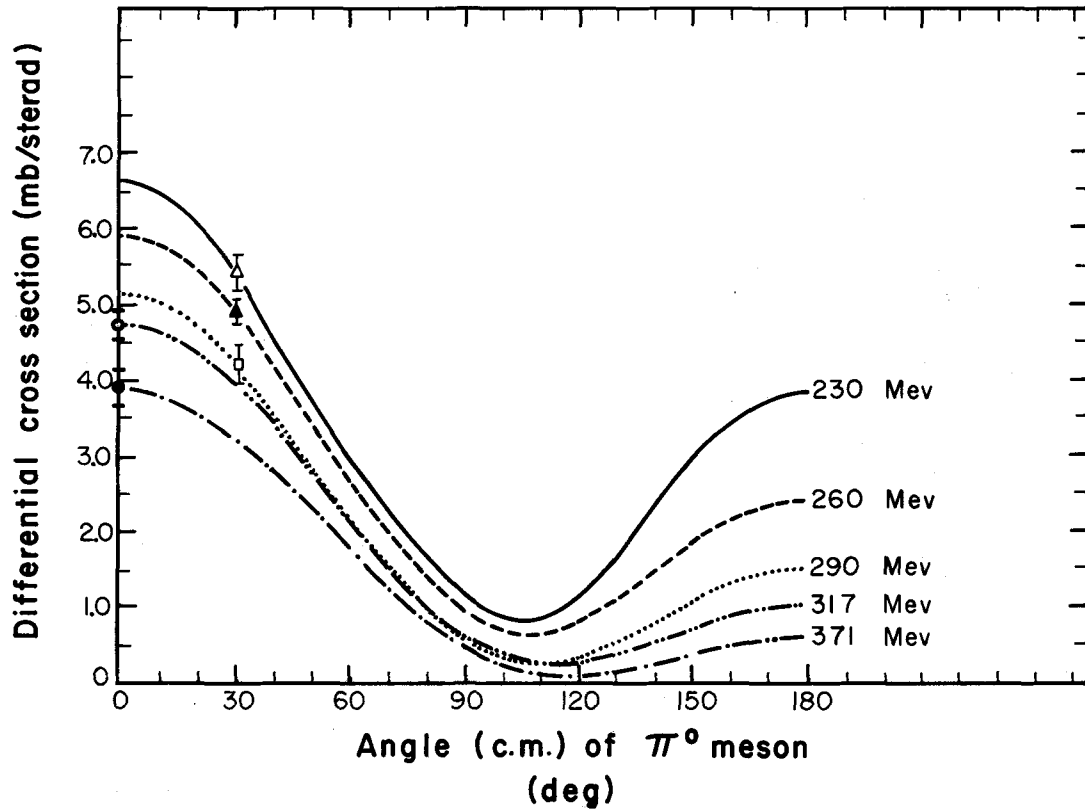
Fig. 18. Coefficient a_3 vs. incident pion kinetic energy.
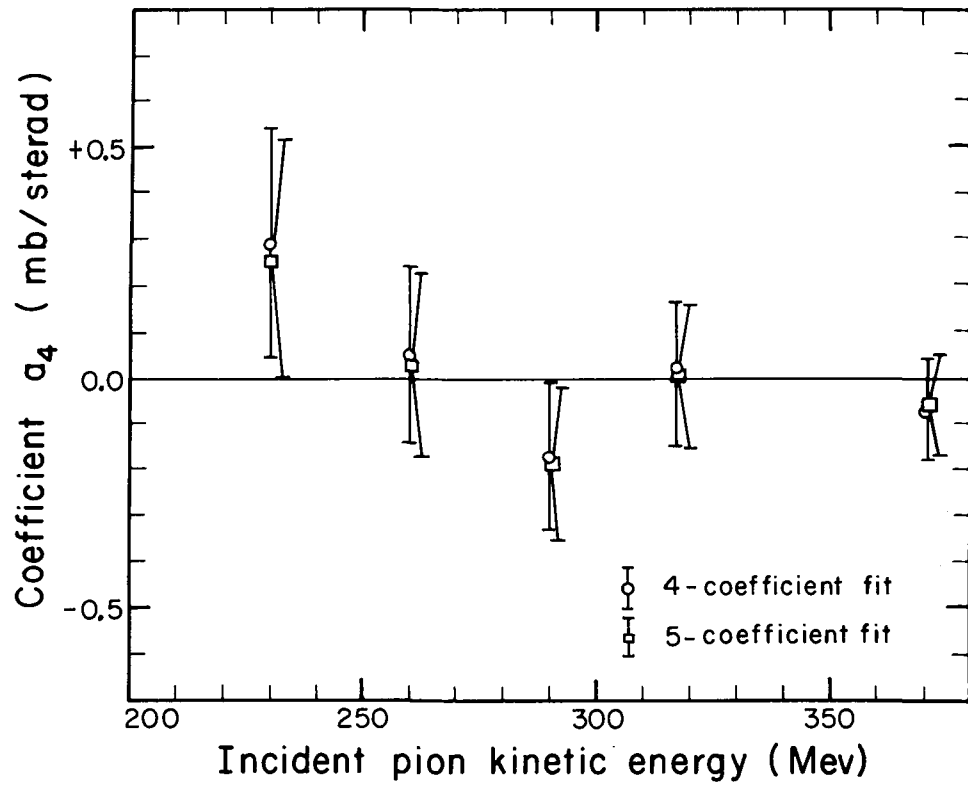
Fig. 19. Coefficient a_4 vs. incident pion kinetic energy for both four- and 5-coefficient fits to the data.

MU-19807

Fig. 20. Coefficient a_5 vs. incident pion kinetic energy for the 5 coefficient fit to the data.

Fig. 21. Charge-exchange angular distributions in the c.m. system computed from the "best fit" coefficients for the three-coefficient fit. The errors shown indicate the size of the error bands.
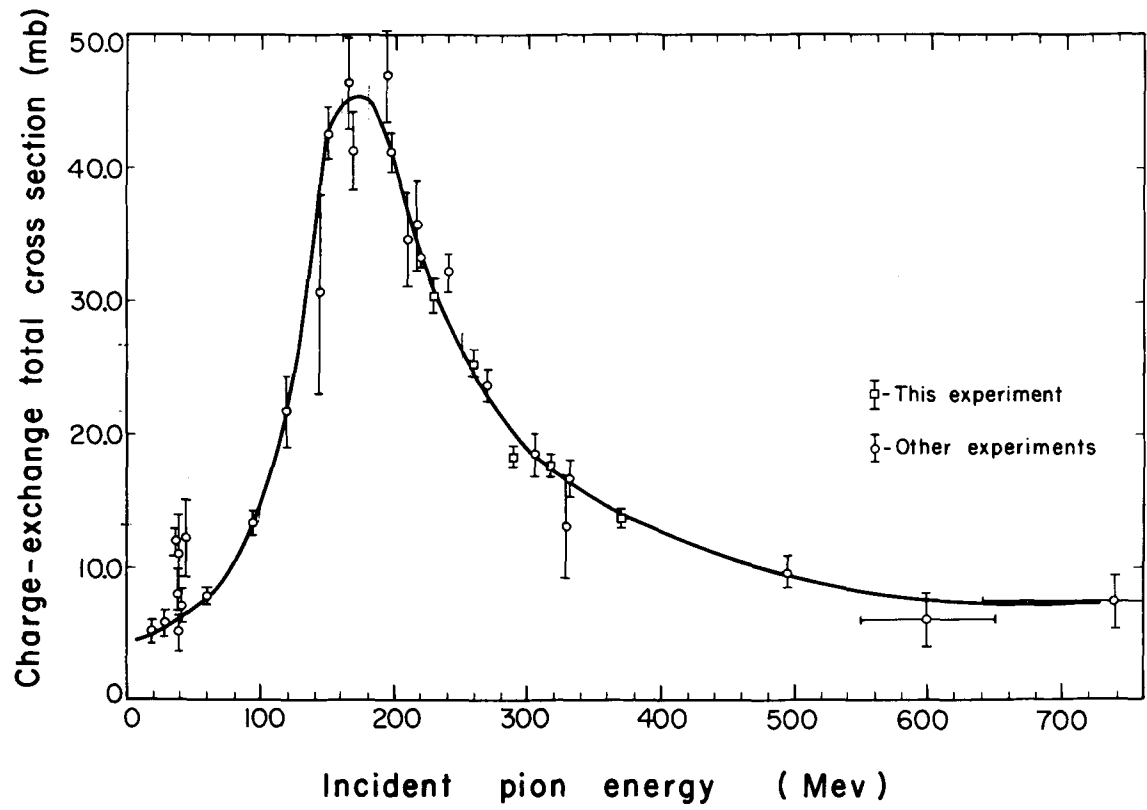
Fig. 22. Charge-exchange total cross section vs. incident pion kinetic energy.

Table XVIII

Charge-exchange total cross section

computed from $\sigma = 4\pi(a_1 \pm \delta a_1)$ mb

Incident pion kinetic energy (Mev)	Total cross section (mb)
230	30.4 ± 1.3
260	25.4 ± 1.0
290	18.2 ± 0.8
317	17.6 ± 0.8
371	13.6 ± 0.6

VI. COUNTER-TELESCOPE CALIBRATION

A. Introduction

The purpose of the gamma-ray counter calibration was to measure by a direct method the absolute detection efficiency as a function of incident gamma-ray energy.

The method we used measures the counter's response to a well-collimated bremsstrahlung beam of various peak energies from the 325-Mev Berkeley synchrotron. Obtaining the efficiency, $\epsilon(k)$, from these measurements is discussed in Sec. VI. D. Absolute efficiency determination depends on accurate measurement of the low-intensity bremsstrahlung beam we used. Monitoring this feeble beam was made possible by a suitable choice of collimators and by using a pair spectrometer as intermediate beam monitor between a thick-walled ionization chamber [19] and the gamma-ray counter (Sec. VI. B).

We also measured the relative counter efficiency as a function of incident beam's position and angle of incidence upon the gamma-ray counter telescope.

B. Experimental Arrangement

Figure 23 shows the experimental arrangement for the counter calibration. The 5/16-in.-diameter lead collimator was found necessary to reduce off-axis beam intensity incident upon the pair spectrometer,

(a) to reduce pair spectrometer accidental counts for a given beam intensity along the beam axis, and

(b) to illuminate the pair spectrometer converter only near the beam axis.

Cornell chambers [19] I and II, thick-walled ionization chambers carrying the bremsstrahlung beam absolute calibration, were identical. Cornell chamber I was used for pair spectrometer cutoff curves and bremsstrahlung spectrum normalization. It was removed from the beam line during measurements of response of the gamma-ray counter and Cornell chamber II. Cornell chamber II was removed from the beam line during counter-response measurements.
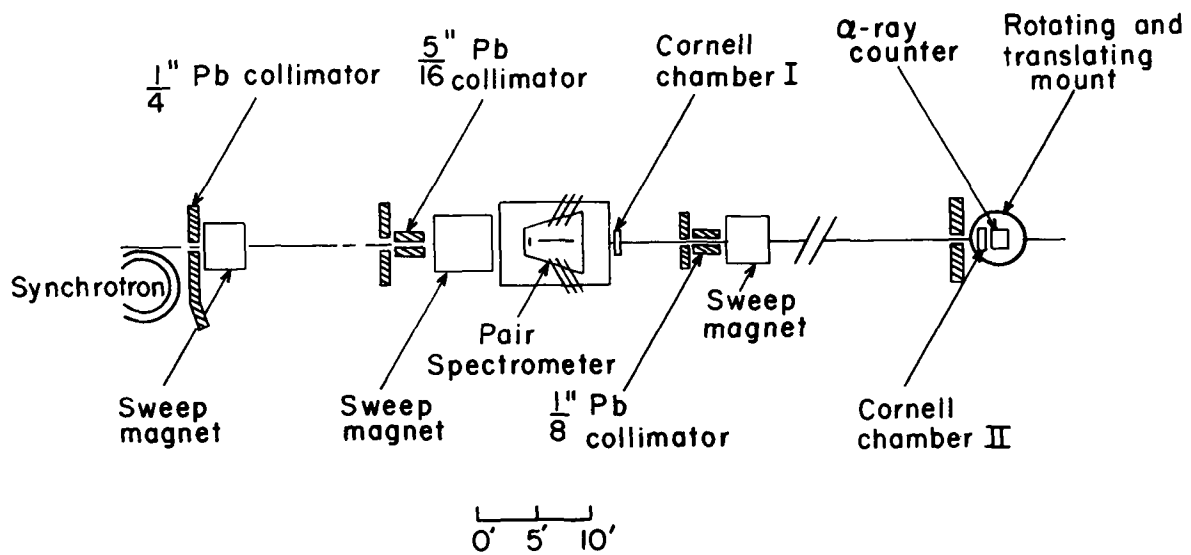
Fig. 23. Experimental arrangement for gamma-ray counter calibration.

The pair spectrometer made possible monitoring of the bremsstrahlung beam over the large range of beam intensity between

(a) the relatively high intensity needed to charge Cornell chamber II at a detectable rate and

(b) the jamming point of the gamma-ray counter at a much lower intensity.

The 1/8-in.-diameter lead collimator permitted transmission of a sufficiently small fraction of the incident beam to allow simultaneous operation of both pair spectrometer and gamma-ray counter. Beam spot diameter incident upon the counter face was less than 1/4 in.

A rotating and translating counter mount permitted measurement of the relative counter efficiency as a function of both beam position and beam angle of incidence upon the counter telescope face.

Sweep magnets downstream from each collimator eliminated electrons from the beam line.

C.   Electronics and Beam Monitoring

Electronic block diagrams for the gamma-ray counter efficiency measurements are shown in Figs. 24, 25, and 26.

The pair-spectrometer multiple-coincidence circuit was a diode-bridge type. Three pair-spectrometer channels were used.

An Evans coincidence circuit[14] was used for the gamma-ray counter telescope.

A Cary Model 31 Vibrating-Reed Electrometer was successfully used to accurately measure the small currents obtained from Cornell chamber II. The Model II Integrating Electrometers one usually finds satisfactory for relatively high currents were unusable. On the most sensitive scales random-drift rates were larger than the currents to be measured. Drift rates of the Cary Vibrating-reed electrometer were negligible in relation to the currents measured.
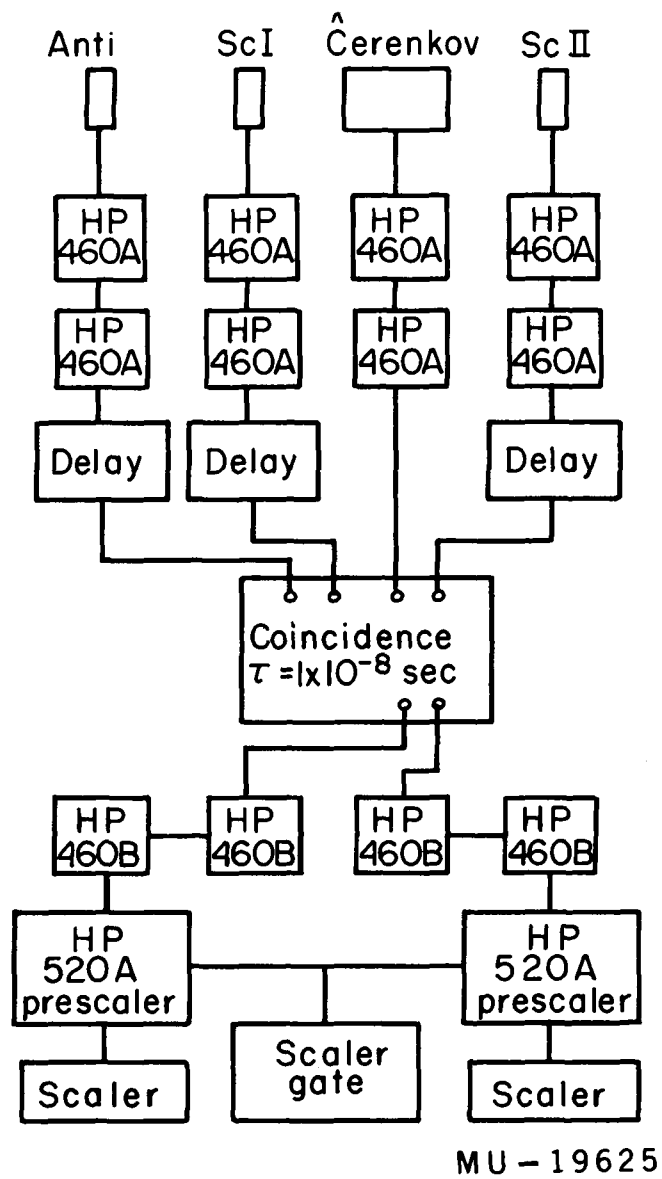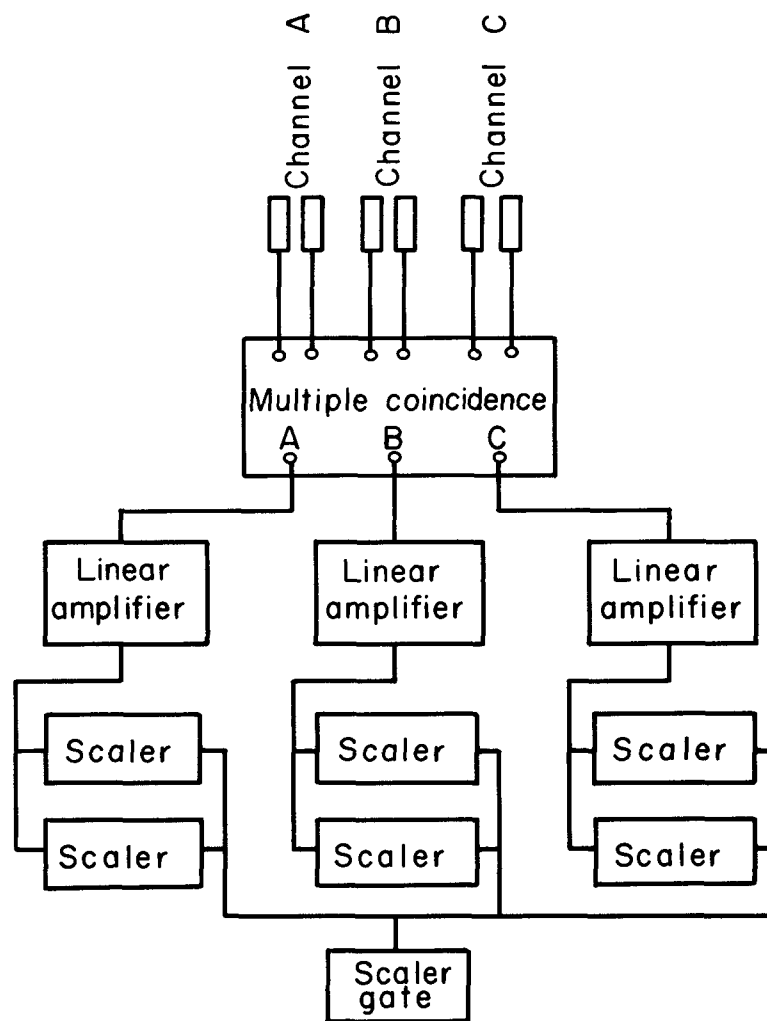
Fig. 24. Gamma-ray counter telescope: electronics block diagram.

MU−19626

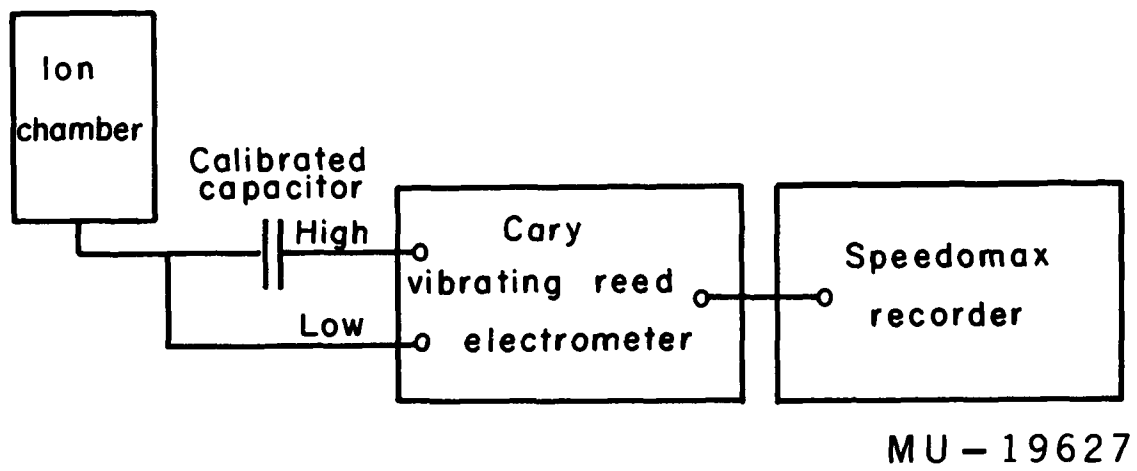Fig. 25. Pair spectrometer: electronics block diagram.

MU − 19627

Fig. 26. Cornell chamber: electronics block diagram.

D. Theory

Appendix B presents a derivation of the relations necessary to obtain the gamma-ray counter efficiency from experimental measurements. The counter efficiency as an explicit function of incident photon energy, k, is given by

$$\epsilon(k) = a \, \ell n \left(\frac{k}{k_{th}} \right) , \tag{19}$$

where a is the parameter to be measured and k_{th} is the measured energy threshold of the counter, in Mev. The parameter a can be related to the measurements by

$$a = \frac{a_i \left[A_i - \ell C_i \right]}{\gamma_i} . \tag{20}$$

Appendix B gives definitions of the factors of Eq. (20).

Our purpose here is to briefly discuss how one evaluates Eq. (20). Experimental techniques are discussed in Sec. IV. E. Experimental and computational results together with the final value for a are presented in Sec. VI. F.

The quantity of γ_i (counts/μcoulomb) was obtained from the product of the experimental ratios

$$\gamma_i = G_i H_i , \tag{21}$$

where

$$G_i = \frac{\text{net } \gamma\text{-ray telescope counts}}{\text{net pair spectrometer counts}} , \tag{22}$$

$$H_i = \frac{\text{net pair spectrometer counts}}{\mu\text{coulombs from Cornell Chamber II}} . \tag{23}$$

Integrals A_i, B_i, and C_i were evaluated by plotting the integrands and measuring the area thereunder by planimeter. The integrands were obtained by using the bremsstrahlung spectra $B_i(k)$ due to Schiff,[20] with the constant C set equal to 111. These spectra were

obtained by integrating the Bethe-Heitler cross section[20] over radiation-straggled angles and photon angles. The Berkeley synchrotron uses a 0.020-in.-thick platinum target (Z = 78). The spectrum used is averaged over photon angles because electron scattering in the platinum target effectively samples all angles of photon emission. Computation of the spectra was performed by IBM 650 computer. The spectra have not been corrected for the energy spread in k_{max_i} due to the spread in beam spill-out time. This energy spread amounts to less than ±0.5%. Figure 27 shows the spectra used.

The constant a_i was obtained from the quotient

$$a_i = N_i / B_i , \qquad (24)$$

where B_i was evaluated by planimeter integration as described above and N_i was obtained from the Cornell chamber calibration curve. Figure 28 shows the most recently reported summary of absolute-response measurements for a Cornell-type thick-walled ionization chamber.[21] The N_i values reported by Fig. 28 are for an air-filled chamber at standard conditions. A 7±1.5% correction to these values was made to account for the temperature and pressure at which our Cornell chamber was filled.

E. Experimental Procedure

The experimental program involved two series of measurements:

(a) a preliminary series to demonstrate that the method would in fact work, and

(b) measurements needed for the analysis described in Sec. VI. D.

The preliminary series involved--in addition to counter plateaus, jamming curves, and delay curves--the following measurements. The experimental-setup geometry, including sizes for the collimator holes, was experimentally determined. We feared the small-diameter collimators might distort a transmitted bremsstrahlung spectrum sufficiently to preclude 2% accurate measurements.
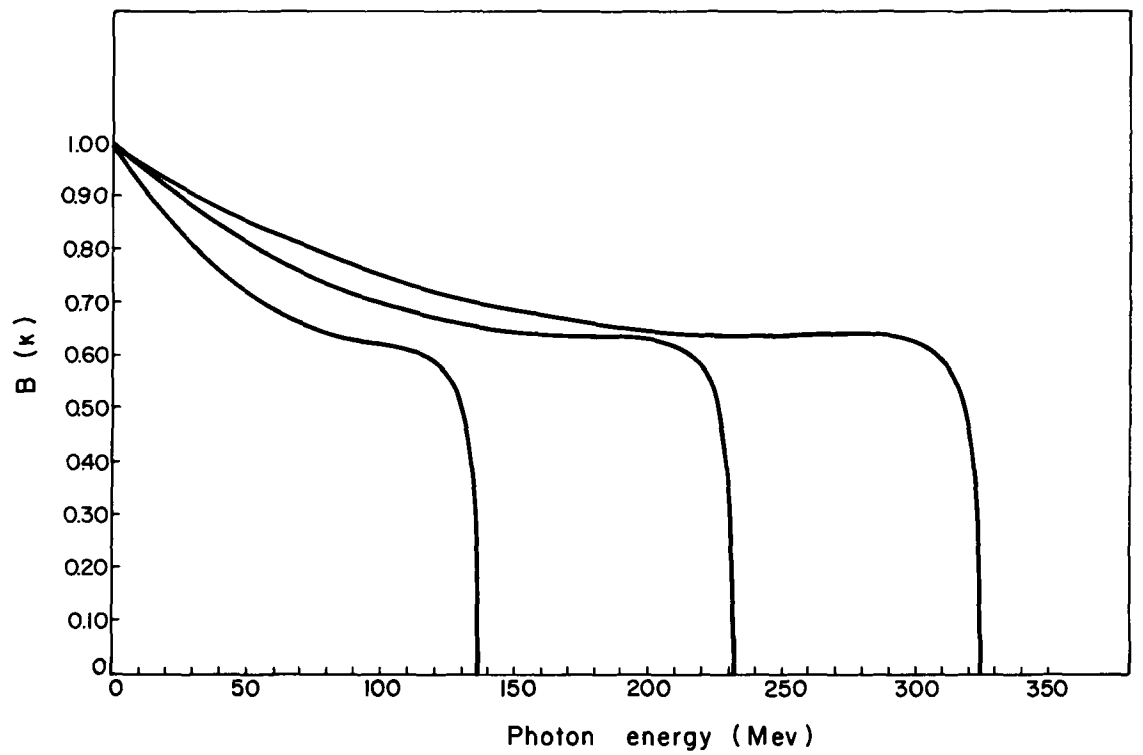
MU-19632

Fig. 27. Bremsstrahlung spectra used for the gamma-ray counter calibration.
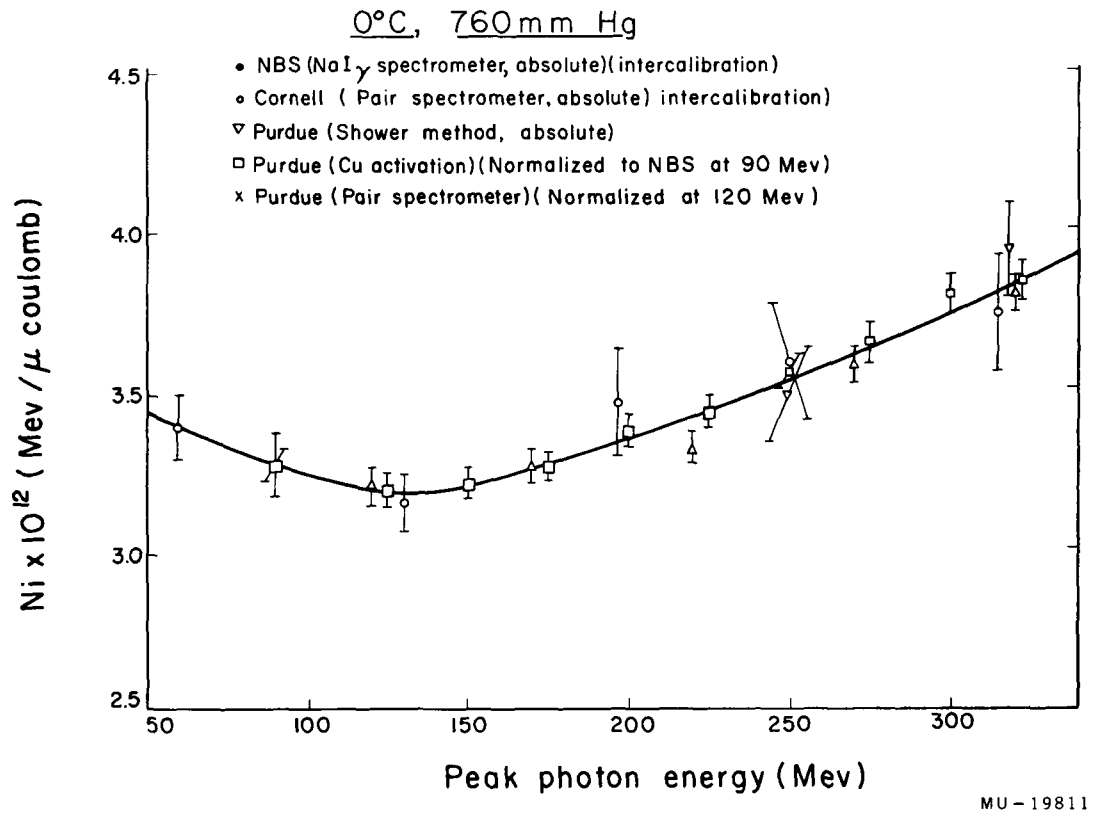
Fig. 28. Cornell chamber calibration curve.

Pair-spectrometer observations proved that a 1/8-in.-diameter Pb collimator did not distort a transmitted spectrum. Statistical counting errors were less than 1% for these measurements, and no systematic errors due to electronic drifts were detected. Our method was to measure two samples of the bremsstrahlung spectrum by pair spectrometer at various energies. One sample was transmitted through a 1/8-in.-diameter Pb collimator and the other sample was observed without collimation. Counting rates from both samples were identical within the statistical counting errors.

The experimental program's second part involved three measurements for each peak energy:

(a) accurate measurement of the peak energy,

(b) measurement of the counting ratio of the gamma-ray counter to the pair spectrometer, and

(c) measurement of the ratio of pair-spectrometer counting to Cornell chamber charging.

Threshold energy of the counter was measured. We also measured the relative gamma-ray counter efficiency as a function of the position and incidence angle of the photon beam upon the counter face. We will briefly discuss each measurement.

Bremsstrahlung peak energies were determined by pair-spectrometer cutoff curves. Figure 29 shows the typical cutoff curve obtained for peak energy K_{max_i} = 232 Mev. Net pair-spectrometer counts plotted on Fig. 29 include correction for accidentals and converter-out counts. The magnetization curve for the 350-Mev pair-spectrometer magnet is given in Fig. 30. Peak photon energy was computed from the relation

$$B\rho = \frac{10^8}{C} \sqrt{T(T+2R)} , \tag{25}$$

where B is the magnetic field, in kilogauss; ρ is the sum of electron and position radii, in cm; T is the electron kinetic energy, in ev; and R is the electron rest energy, in ev. Solving for the kinetic energy, we have

$$T = R \pm \sqrt{R^2 + 9 \times 10^4 B^2 \rho^2} . \tag{26}$$

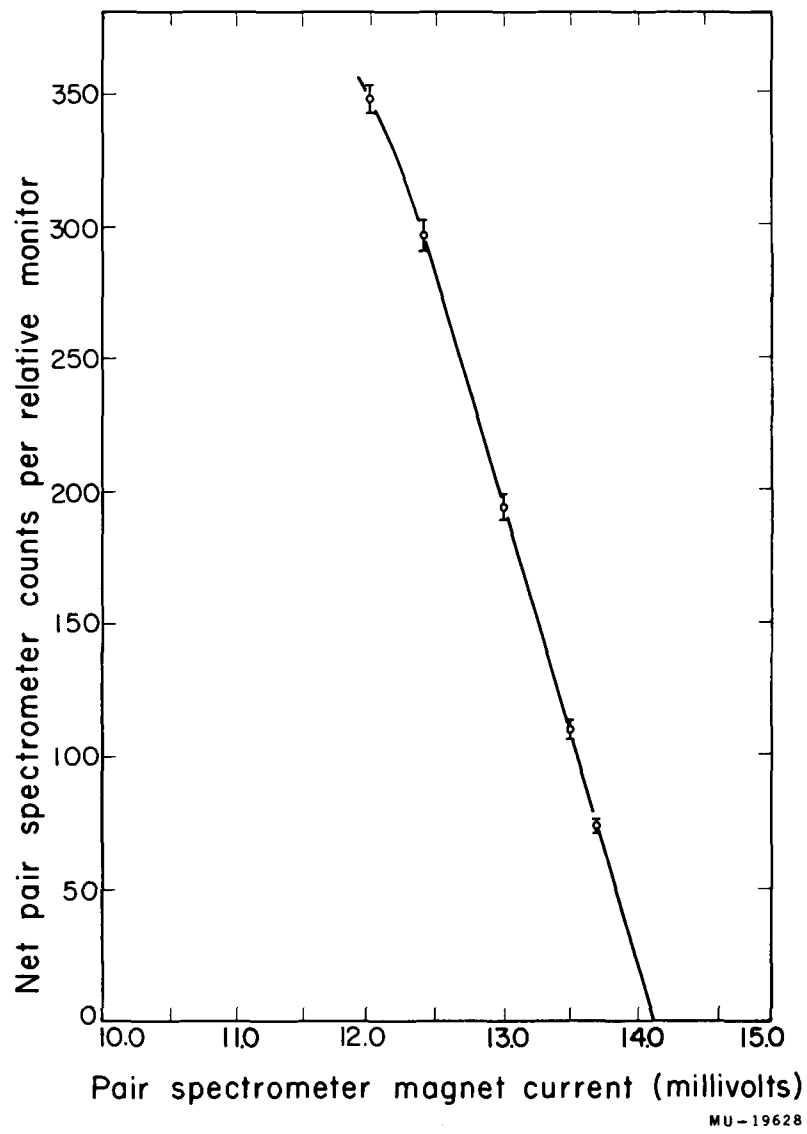The energy needed to create an electron pair was added to T to obtain peak photon energy, K_{max_i}.

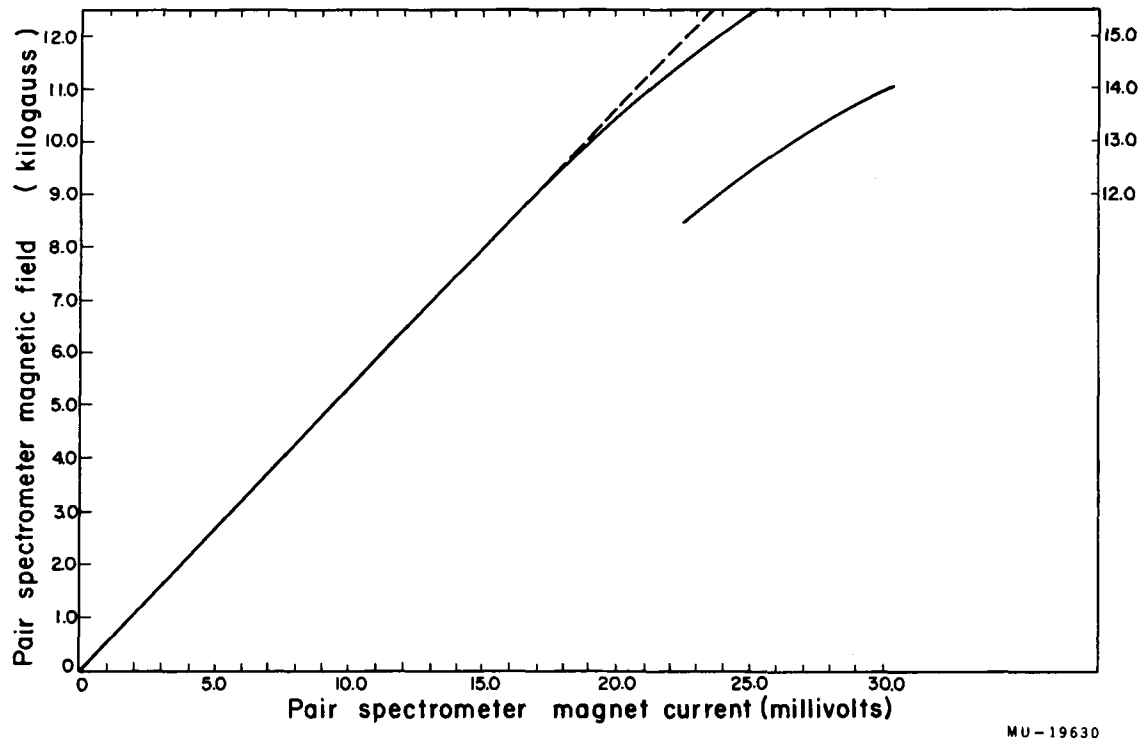**Fig. 29.** Pair spectrometer cutoff curve for K_{max_i} = 232 Mev.

Fig. 30. Pair spectrometer magnetization curve.

The ratio of gamma-ray counter to pair spectrometer was independent of incident flux. Approximately 0.1% of the flux incident on the pair spectrometer was transmitted by the 1/8-in.-diameter Pb collimator. The net measured ratio was corrected for pair-spectrometer accidentals and gamma-ray counter accidental and converter-out counts. Cornell chamber II was removed from the beam line during this measurement. Gamma-ray count rate with the 1/8-in. collimator blocked was found to be zero.

The ratio of pair spectrometer to Cornell chanber was measured with a photon flux approximately 100 times as intense as for the previous ratio. Such flux increase was needed to charge Cornell Chamber II at a measurable rate. The pair spectrometer was operated under identical conditions for both ratio measurements. No systematic drifts were detected.

Figure 31 shows the observed gamma-ray counting rate as peak bremsstrahlung energy was reduced by causing the synchrotron electron beam to fall out before peak field. Beam-fall-out delay from peak field was measured by a Model 545 Tektronix scope whose time scale was checked against a standard oscillator. Counter energy threshold was computed from

$$K = K_{max} \sin \left[90° \left(\frac{7820 - T}{7820} \right) \right] , \tag{27}$$

where 7820 μsec is the measured time to peak field; T is the measured delay from peak field, in μsec; and K is the bremsstrahlung peak energy corresponding to T.

Figure 32 shows relative gamma-ray counter efficiencies measured as a function of incident-beam position and incidence angle on the counter face. Incident-beam diameter was less than 1/4 in.
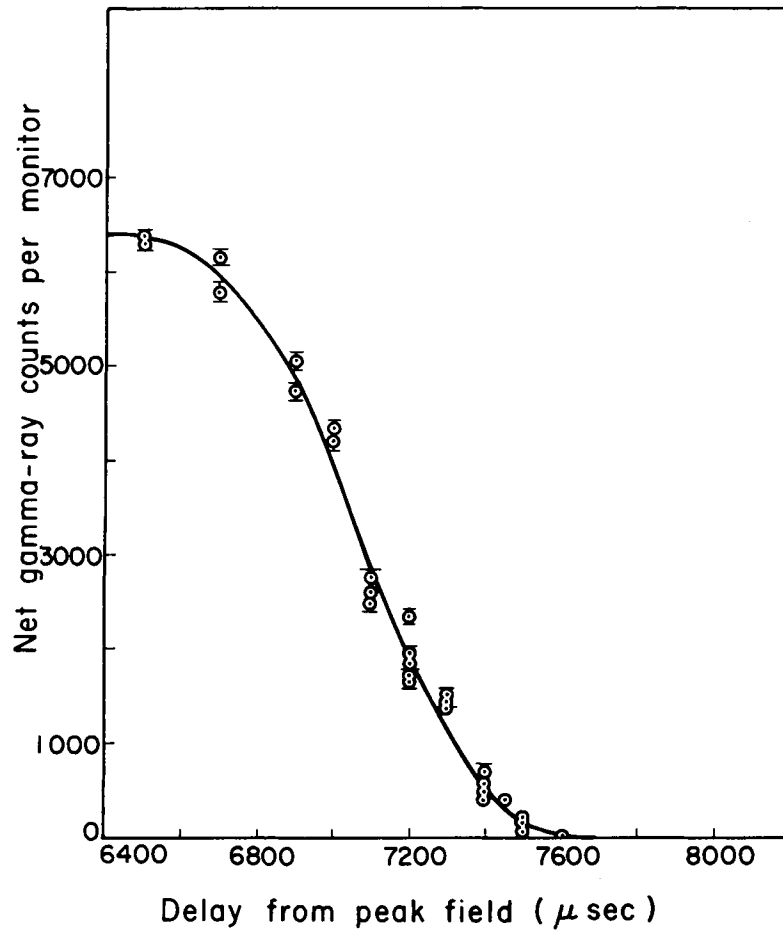
Fig. 31. Gamma-ray counter response curve used to measure the counter threshold energy.
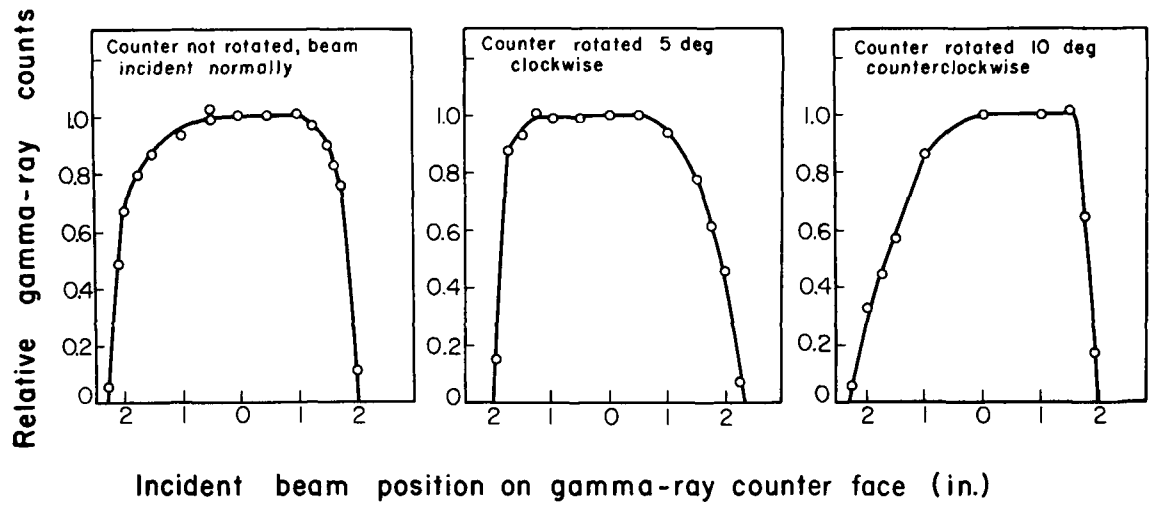
Fig. 32. Relative gamma-ray counter efficiency measurements as a function of incident beam position and incidence angle.

F. Results

We present in Table XIX the experimental results and the results of the analysis based on those measurements. Table XX shows the results for measurment of peak energy.

The weighted average of the individual values for a_i is $a = 0.136 \pm .007$. The gamma-ray counter efficiency is

$$\epsilon(k) = (.136 \pm .007) \, \ln \left(\frac{k}{13.5 \pm 0.50} \right) . \tag{28}$$

Table XIX

Results of peak energy determinaton				
Cutoff (Mev)	Cutoff (kilogauss)	T (Mev)	K_{max_i} (Mev)^i	K_{max_i} corrected for beam-fallout width
8.24±.05	4.04±.04	135±1.6	136±1.6	136±1.7
14.13±.03	7.50±.03	231±1.5	231±1.5	232±1.6
20.12±.05	20.12±.05	323.9±2.3	324±2.3	325±2.6

$\rho = 102.79 \pm .23$ cm.

$R = 0.511 \pm .001$ Mev

Table XX

	Gamma-ray counter calibration results		
	Peak energy (Mev)		
Quantity	136	232	325
γ_i/Cornell	$(8.29\pm.29)\times10^9$	$(9.57\pm.53)\times10^9$	$(8.88\pm.38)\times10^9$
a_i	$(3.58\pm.10)\times10^{10}$	$(2.22\pm.06)\times10^{10}$	$(1.76\pm.05)\times10^{10}$
$\left[A_i - \ell C_i\right]$	$1.85\pm.18$	$2.90\pm.18$	$3.77\pm.18$
α_i	$0.126\pm.014$	$0.149\pm.013$	$0.134\pm.009$

VII. CORRECTIONS

This section classifies the corrections into two groups:
(A) those applied to the observed counting rates, and (b) those applied
to the experimental geometry. Correction for pion beam contamination
is discussed in Sec. II. B.

A. Counting-Rate Corrections

In any given experimental arrangement accidental counts
usually arise from more than one source. Our experiment had two
possible sources of accidental gamma-ray counts: (a) random-noise
accidentals due to high singles rates in the various coincidence channels,
and (b) "beam bunching" accidentals due to more than one incident pion
per beam fine-structure bunch. Random-noise accidentals were shown
by calculation to be negligible. The calculations were based on mea-
sured singles rates in each coincidence channel, coincidence resolving
times, and beam duty factors. The second type of accidental arises
from the monitor coincidence circuit's inability to resolve two incident
pions within less than 1×10^{-8} sec, i. e., more than one incident pion
per fine-structure bunch. Since each incident pion may produce an
observed gamma-ray and only one incident pion is detected, accidental
counts arise.

In a high-counting-rate experiment, measurements of the
accidentals made by inserting delay lines may not determine the true
accidental rate. To justify our correction method we make the following
argument. The cyclotron beam fine structure is determined by the final
proton frequency and the circumferential spread of the phase-stable bunch.
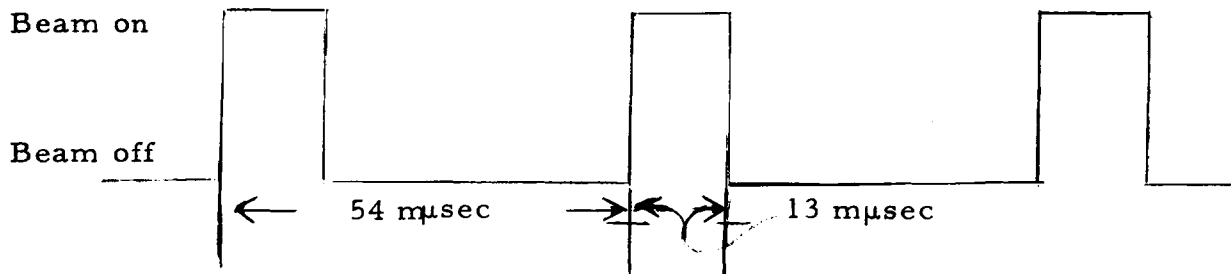Figure 33 diagrams the cyclotron beam fine structure.

Fig. 33. Cyclotron beam fine structure.

This fine-structure pattern continues for 400 μsec total fall-out time at a repetition rate of 64 per sec. Knowing the average incident pion flux, one can easily compute the probability for finding more than one pion per fine-structure bunch and the accidental gamma-ray counting rate corresponding to this probability. The computed accidental counting rates agreed very closely with the accidental counting rates measured by delaying the monitor coincidence one fine-structure time, 5.4×10^{-8} sec, relative to the gamma-ray counter.

We corrected for gamma-ray counts lost owing to (a) photon attenuation in the aluminum vacuum jacket surrounding the liquid hydrogen container and (b) the Dalitz process,

$$\pi^0 \to \gamma + e^+ + e^-, \tag{29}$$

by which 0.73 % of the gamma rays are replaced by an electron pair.[22] Photon attenuation was computed in consideration of the photon spectrum observed at each laboratory-system angle. We found that an average attenuation valid for all energies and all angles is 0.70% ± 0.30%. The total gamma-ray loss due to both processes is estimated as 1.4% ± 0.5%.

The radiative capture process,

$$\pi^- + p \to n + \gamma, \tag{30}$$

makes a small contribution to the observed counting rates. Knowing the negative-to-positive pion photoproduction ratio from deuterium[23] and the differential cross section for positive pion photoproduction from hydrogen,[24,25] we estimated the radiative capture cross section in the c.m. frame by detailed balancing,

$$\left(\frac{d\sigma}{d\omega}\right)_{\pi^- + p \to \gamma + n} = 2 \left(\frac{\pi^-}{\pi^+}(\theta)\right) \left(\frac{P_\gamma}{P_{\pi^+}}\right)^2 \left(\frac{d\sigma}{d\omega}\right)_{\gamma + p \to \pi^+ + n}. \tag{31}$$

We used this cross section to estimate the corresponding laboratory-system counting rates.

The inelastic reactions

$$\pi^- + p \to n + \pi^0 + \pi^0,$$
$$\pi^- + p \to p + \pi^- + \pi^0 \tag{32}$$

also make a small contribution to the gamma-ray counting rate. We estimated this contribution by assuming (a) that the π^0 angular distribution is isotropic and (b) that the total cross section for each reaction is equal to that measured for

$$\pi^- + p \rightarrow n + \pi^- + \pi^+ \tag{33}$$

by Perkins.[17]

B.   Geometrical Corrections

Geometrical corrections were made to the quantities $G, \Delta\Omega$, and nt of Eq. (A15) (Appendix A).

The factor G accounts for variation of the differential cross section for gamma-ray production over the range of angles detected at a given counter setting. Perkins has reported a detailed discussion of our computation method for G.[17] This factor was found negligibly different from unity for all observation angles. Figure 34 shows the target and counter geometry used as a basis for the geometric corrections.

The corrected solid angle, $\Delta\Omega$, is given by

$$\Delta\Omega = \frac{A}{d^2} (1 + a), \tag{34}$$

where A is the Pb converter's effective area in cm^2, d is the distance from Pb converter to hydrogen target center in cm, and a is the first-order solid-angle correction factor. Both factors a and G were computed by using IBM 650 programs. The Pb converter effective area, A, is 14.5% less than the geometrical area. This correction accounts for the decrease in detector efficiency for photons incident upon the counter face off center and off normal.

The target thickness, nt, is corrected for (a) variable target thickness due to bowing of the walls of the liquid hydrogen vessel, and (b) the appreciable variation of beam intensity with beam radius as shown by the beam profile measurements. The average target thickness is
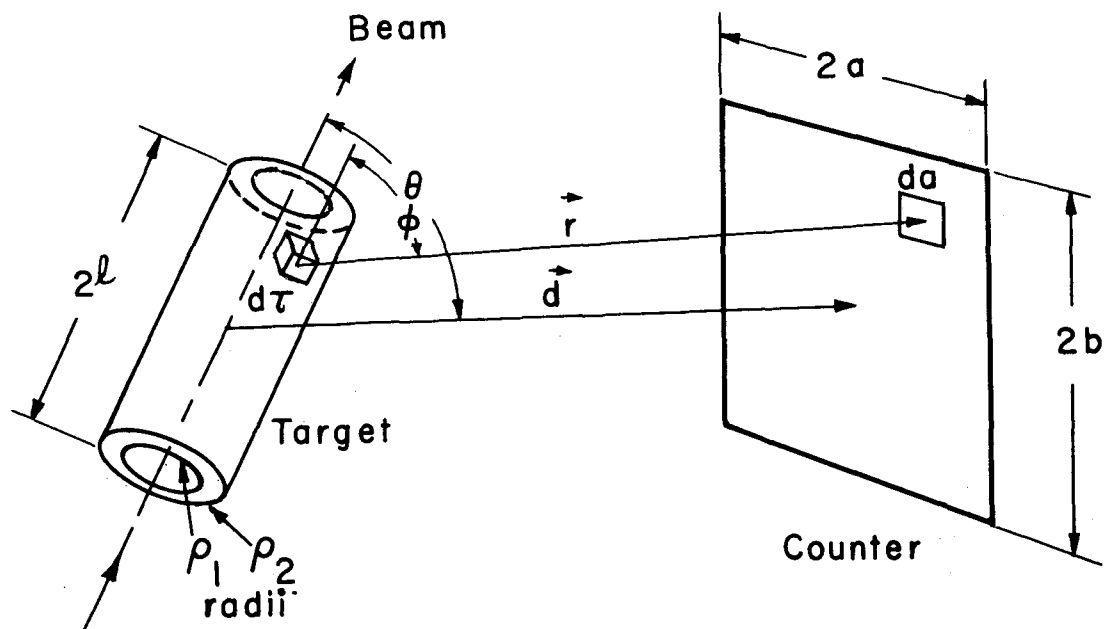
MU−17556

Fig. 34. Target and counter geometry used as a basis for geometric
corrections.

$$nt = n \frac{\iint \rho(r)t(r,\theta)rdrd\theta}{\iint \rho(r)rdrd\theta} , \qquad (35)$$

where $\rho(r)$ is the beam profile in relative units, $t(r,\theta)$ is the hydrogen vessel thickness in cm, and n is the liquid hydrogen density in protons/cm^3. The integrals of Eq. (35) were evaluated by a summation approximation made by dividing the beam profile into concentric rings about the beam axis and the circumference of each ring into quadrants,

$$\iint \rho(r)rdrd\theta \approx \pi \sum_i \rho(r)(r_i^2 - r_{i-1}^2) , \qquad (36)$$

$$\iint \rho(r)t(r,\theta)rdrd\theta \approx \frac{\pi}{4} \sum_i \sum_j \rho(r)(r_i^2 - r_{i-1}^2)t(r_i,\theta_j), \qquad (37)$$

where the index i denotes the ith ring, the index j denotes the jth quadrant, $r = \frac{r_i + r_{i-1}}{2}$, and $t(r_i,\theta_j)$ is the average target thickness in the interval $\Delta r_i \Delta \theta_j$. The target thicknesses (in cm) were measured by micrometer by using the grid of dots on the hydrogen vessel walls. The average target thickness is $(4.59\pm0.09) \times 10^{23}$ protons/cm^2. This number is valid for the hydrogen vessel at liquid hydrogen temperature and includes a 1% correction for the residual hydrogen gas present during target-empty measurements.

VIII. DISCUSSION OF RESULTS

Our purpose in this section is to discuss the results contained in Tables VIII, IX, X, XI, and XII in terms of the evidence for the presence of d-wave scattering. Our discussion is motivated by the total lack of evidence for d-wave scattering in charge-exchange reaction to date. The only other work in our energy range, by Korenchenko and Zinov,[12] reports no coefficients a_4 and a_5. These gentlemen analyzed their experiment by the approximate method outlined at the beginning of our Sec. IV. In their analysis of the 240- 270-, and 307-Mev experiments they included only s- and p-wave scattering. At 333 Mev they made two fits to their data. The first fit, a 3-coefficient fit, assumed only s- and p-wave scattering and yielded a least-squares sum $S = 1.51$. The second fit, a 5-coefficient fit, included provision for d-wave scattering also. Their result was $b_4 = 0.18\pm0.63$, $b_5 = 0.04\pm.54$ and $S = 1.27$, where b_4 and b_5 are coefficients of the gamma-ray differential cross section of Eq. (7). They correctly state that no conclusion could be drawn concerning d-wave scattering from this result. Thus, when they inverted the gamma-ray differential cross section to obtain the charge-exchange differential cross section of Eq. (8), only s-and p-waves were considered. It is unfortunate that they applied to their results no statistical goodness-of-fit criteria other than the least-squares sum value. Any additional evidence we can report will assist the resolution of the problem. We have performed a 1-, 2-, 3-, 4-, and 5-coefficient fit of Eq. (8) to the data at each energy. Two statistical goodness-of-fit tests have been applied to these results.

As background for this discussion we recall to mind the following points. The experimental charge-exchange scattering data have been fitted to the function

$$\frac{d\sigma}{d\Omega} = \sum_{\ell=1}^{5} a_\ell P_{\ell-1}(\alpha) . \tag{8}$$

From the physics of the angular distribution we can readily show which orbital angular momentum states contributes to a given coefficient a_ℓ. We find that:

> s and d waves contribute to a_1;
>
> s, p, and d waves contribute to a_2;
>
> p waves only contribute to a_3;
>
> p and d waves contribute to a_4; and
>
> d waves only contribute to a_5.

We have of course assumed that orbital angular momentum states higher than the d state are absent.

It is reasonable to expect that the contribution of d-wave scattering to coefficients a_1 and a_2 is insignificant relative to the s- and p-wave contributions. Therefore, nonzero coefficients a_5 or a_4(or both) would constitute the most direct evidence for the presence of d-wave scattering. Without considering in detail the extremely complicated expressions for a_4 and a_5 in terms of scattering phase shifts, we can observe from basic physics that

> 1. coefficient a_4 arises from p-and d-wave interference, and thus the d-wave phase shifts appear in its expression to first order only, and
>
> 2. coefficient a_5, being a pure d-wave term, is expressed in terms of d-wave phase shifts to the second order.

With this introduction we discuss the results of the tables mentioned above and Figs. 19 and 20 (See Sec. V). Figure 19 shows our results for coefficient a_4 as a function of incident pion kinetic energy for both a four- and a five-coefficient fit to the data. Figure 20 shows our results for coefficient a_5 as a function of incident pion kinetic energy for a five-coefficient fit to the data. As for as coefficient a_4 is concerned Fig. 19 shows virtually identical results whether or not the fifth coefficient is added to the fitting function, Eq. (8). Unfortunately neither the a_4 nor a_5 coefficient is statistically nonzero with high probability, even at the highest energy.

To extract additional information concerning the adequacy
or goodness of the fits to our data we have performed two related statis-
tical goodness-of-fit tests. The first is the Pearson chi-squared test,[26,27]
and the second is the so-called F test,[27] which supplements the χ^2 test.
We will discuss each test briefly.

The object of the χ^2 test is to obtain a criterion for the
number of coefficients that must be included in the fitting function to
adequately fit the data. The necessary quantities for the test are

$$\chi^2 = S/\sigma^2 = S \tag{38}$$

and

$$K = N - \ell - 1, \tag{39}$$

where S is the least-squares sum of weighted residuals, σ is the variance
of a function of unit weight, K is the number of degrees of freedom, N is
the number of observation angles, and ℓ is the number of coefficients of
Eq. (8) used to fit the data. The value of χ^2 and the number of degrees
of freedom, K, define a probability P -- the probability that the value of
χ^2 should exceed the value obtained by assuming a given fitting function.
According to Cziffra and Moravscik,[27] the value of P will in general
reach a plateau value as ℓ, the number of coefficients used in the fitting
function, is increased. The value of P is generally rather insensitive to
the number of coefficients once the plateau values have been reached.
Thus the number of coefficients needed for the "best" fit is the smallest
ℓ value on the plateau.

The plateau value of P may be used to decide whether the
"best" fit indicated by the plateau is indeed a good fit. According to
Evans[26] we may interpret the value of P by considering that:

    (a) the assumed function very probably corresponds to the
        observed one if P lies between 0.10 and 0.90 (1.65 standard
        deviations),

    (b) the assumed function is extremely unlikely should P be
        less than 0.02 or more than 0.98 (2.35 standard deviations).

Of course these values are somewhat arbitrary, depending on the confi-
dence levels one wishes to use. To summarize the first statistical test,
the Pearson χ^2 test, we say that if affords a method for obtaining a

"best" fit and deciding if this fit is indeed a good fit. It would be desireable to also have an auxiliary test to tell us the probability that we were correct in assuming that the coefficients a_l for l greater than the smallest plateau value ("best" fit value) are indeed zero.

The second statistical test, the so-called F test,[27] is just such a test used to corroborate the χ^2 test. The F test gives the probability, on the basis of the available data, that a given $a_l = 0$. We will briefly outline the F test according to Cziffra and Moravscik.[27]

One evaluates the quantity

$$S(K) = \frac{K}{S_l} (S_{l-1} - S_l), \tag{40}$$

where K is the number of degrees of freedom corresponding to l, and S_l and S_{l-1} are the observed least-squares sums of weighted residuals for fits using l and $l-1$ coefficients, respectively. The quantities S_l and $(S_{l-1} - S_l)$ obey a χ^2 distribution with K degrees of freedom and one degree of freedom, respectively. The distribution of two χ^2 variables divided by their respective degrees of freedom is defined as a Fisher distribution, $F(k_1, k_2)$, where k_1 and k_2 are the number of degrees of freedom of the numerator and denominator, respectively. Therefore S(k) has an $F(1, K)$ distribution. The probability P for

$$S(K) \geq F_p(K) \tag{41}$$

may be shown to be

$$p = \int_{F_p(K)}^{\infty} F(1, K) \, dF. \tag{42}$$

To apply the F test in practice one states that for $S(K) \geq F_p(K)$ one may assume $a_l = 0$ with a probability P of being correct in this assumption. Cziffra and Moravscik present a table giving values of $F_p(K)$ for a given value of K and p.[27] To conclude our discussion of the tests we note that even if the F test indicates with high probability that a_l is 0, it is still

possible that $a_{\ell+1}$, $a_{\ell+2}$. etc. are not zero. However, if the F test is always used in conjunction with the χ^2 test one need not fear terminating the fitting function prematurely.

To perform these statistical tests we used the LSMFT program to compute a fit of our results to Eq. (8) for five cases:

(a)   an s-wave fit using one coefficient (a_1),

(b)   an s- and p-wave fit using two coefficients (a_1 and a_2).

(c)   an s- and p-wave fit using three coefficients (a_1, a_2, and a_3),

(d)   an s-, p-, and d-wave fit using four coefficients (a_1, a_2, a_3, and a_4),

(e)   an s-, p-, and d-wave fit using five coefficients (a_1, a_2, a_3, a_4, and a_5).

Table XXI presents the results of the χ^2 and F tests. We observed that at each energy the χ^2 probability, P, does indeed reach a definite plateau at $\ell = 3$, i.e., a three-parameter fit is the "best" fit. The absolute values of P on the plateaus indicate that at each energy the "best" fit is indeed a good fit. The values of χ^2 are decidely less than their expection value, K, at each energy. This indicates that the experimental errors on the coefficients have been reported conservatively.[27] There is, as expected, a less than 1% probability at each energy that less than a three-coefficient fit is adequate. The results for the one- and two-coefficient fits are included to dramatically show the plateaus. We also note the relatively insensitive behaviour of the χ^2 probability for $\ell \geqslant 3$. If there were an increase in the importance of d-wave scattering with increasing energy one might expect to see a trend towards higher values of P for $\ell=4$ and $\ell=5$ fits relative to the P values for $\ell=3$ fits. Table XXI shows no such trend in the P values except at the lowest energy, 230 Mev, where there is no evidence for d-wave scattering in any π-p reaction. Finally, we observe that at each energy the F test probability P indicates:

(a)   a less than 0.1% probability that coefficient $a_3=0$, and

(b)   reasonable probabilities that coefficients $a_4=a_5=0$.

Table XXI

Energy (Mev)	Number of parameters used for fit, ℓ	Degrees of freedom K	χ^2	χ^2 probability P	F-test probability p
230	1	8	183.7	<< 0.01	--
	2	7	85.35	< 0.01	0.03
	3	6	2.41	0.85	<<0.001
	4	5	1.09	0.93	0.07
	5	4	0.89	0.91	0.35
260	1	7	299.3	<< 0.01	--
	2	6	93.29	< 0.01	0.02
	3	5	1.62	0.90	<<0.001
	4	4	1.56	0.80	0.90
	5	3	1.35	0.75	0.55
290	1	7	462.9	<< 0.01	--
	2	6	107.7	<0.01	0.005
	3	5	2.03	0.81	<<0.001
	4	4	0.94	0.90	0.08
	5	3	0.82	0.83	0.55
317	1	7	514.2	<< 0.01	--
	2	6	82.4	< 0.01	0.001
	3	5	1.67	0.87	<<0.001
	4	4	1.65	0.79	0.85
	5	3	0.93	0.80	0.20
371	1	8	660.5	<< 0.01	--
	2	7	94.23	< 0.01	0.001
	3	6	4.47	0.60	<<0.001
	4	5	4.12	0.52	0.60
	5	4	3.80	0.40	0.65

Results of the Pearson χ^2 test and the F test

Thus we can only conclude that,

(a) only s- and p-wave scattering adequately fit our measurements, and

(b) the presence of d-wave scattering is rather unlikely.

The F-test values give us a quantitative measure of the probability that d-wave scattering is negligible. However, we should note that the F test is derived by assuming that the variables are normally distributed, that they obey an underlying physical law expressible in an infinite series, and that a large number of terms of the series are included in the analysis.[27] Therefore, the F-test values are only partly quantitative since one has no formalism to test how closely these assumptions are satisfied in any given case.[28]

IX. CONCLUSION

We conclude on the basis of the statistical tests described
in Sec. VIII that only s and p waves are necessary to adequately fit our
measurments from 230 to 371 Mev.

There appears to be no need to include d-wave scattering to
fit charge-exchange experiments up through 371 Mev. The published
results below 220 Mev, the results of Ashkin et al. at 220 Mev,[11] the
results of Korenchenko and Zinov from 240 to 333 Mev,[12] and the
results of this experiment establish this statement.

The π^--p elastic scattering and π^+-p scattering measurments
in our energy range appear to require d waves for adequate interpretation.
A very brief summary of the results of these experiments is:

1. Goodwin et al.[29] require d waves for the π^--p elastic
    scattering at 290, 371, and 427 Mev but not at 230 Mev;[29-33]

2. Korenchenko and Zinov, for the π^--p elastic scattering
    reaction, show in their analyses at 307 and 333 Mev a
    slight preference for a d-wave fit, but their result is not
    conclusive;

3. Foote, et al.[31] showed in the analysis of their recent
    π^+-p scattering experiment at 310 Mev, which included
    measurement of the recoil proton polarization, that d waves
    were necessary for obtaining an adequate fit to the data.

These most recent results raise the interesting question, Why
are d waves not found necessary to fit adequately all three π-p reactions at
300 Mev and above ? Of course, the results are not inconsistent with the
possibility that the effect of the d-wave phase shifts for charge-exchange
scattering just cancels out, or that the effects of other π^0-meson-producing
reactions cancels the d-wave contribution. Another possibility is that a
significant relative error exists among the various experiments. The
author thinks the latter possibility rather unlikely, and presents the
following comments to partly support this opinion. We recall that the
work of Goodwin and this experiment were performed simultaneously at
230 and 290 Mev. The 371-Mev measurements of both experiments were
not simultaneous but were performed by using identical pion beams, the
same hydrogen target and the same auxiliary equipment, and operating

techniques standardized within our research group. Both the π^--p
elastic scattering and π^--p charge-exchange total cross sections and
angular distribution coefficients agree well with independent measure-
ments of their respective reactions. Goodwin and the author have
standardized the methods of interpreting the statistical goodness-of-fit
criteria. These factors taken together tend to argue against significant
relative errors.

A few remarks germane to the position of these experiments
relative to future research programs are perhaps appropriate. Future
experimental work on charge-exchange scattering could, in the author's
opinion, take at least three approaches, but only one seems to afford
promise in assisting to answer the d-wave question posed by this experi-
ment. The three approaches are:

    (a) to attain greater accuracy in the differential cross section,

    (b) to extend the differential-cross-section measurements to
        higher energies,

    (c) to measure the recoil-nucleon polarization.

We have been able to reduce the size of errors previously
reported [1,2] only by considerable effort in calibrating the gamma-ray
counter to ±5.3% accuracy, by electronic computer analysis using the
more exact expressions, and by a painstaking program of correction.
The author feels that a significant further reduction of the errors on co-
efficients a_4 and a_5 will not be easily attained.

To extend charge-exchange experiments by counter techniques
to energies above 400 Mev one must solve the difficult experimental problem
of differentiating between gamma rays from the charge-exchange reaction
and those arising from the inelastic π^0-meson production processes (22)
and (23). The kinematic problem of a three-body final state which sub-
sequently decays into photons is, to say the least, formidable. We
estimated these processes as a 3% to 10% correction to our 371-Mev
angular distribution. Therefore, precision work by our method above
400 Mev depends on accurate correction for the inelastic processes. One
can discriminate against much inelastic background on a kinematic basis
by using two gamma-ray counters to count gamma-gamma coincidences.

However, the estimated counting rates are not adequate for precision work, owing especially to solid-angle factors and the relatively low efficiency of each gamma-ray counter.

Recoil-nucleon polarization measurements seem to me likely to yield the greatest amount of useful information for a given amount of experimental effort. To date few recoil-nucleon polarization measurements have been made. Polarization data have been extremely useful in selecting various sets of phase shifts that were otherwise indistinguishable.[31]

A theoretical approach to the d-wave problem is of course the phase-shift analysis. The π^+-p scattering, being pure I = 3/2 state, requires three charge-independent phase shifts for s-and p-wave scattering and five phase shifts if d-wave scattering is included. Analysis of the π^--p reactions is considerably complicated by the presence of both isotopic spin states I = 3/2 and I = 1/2. Ten charge-independent phase shifts are necessary to include s-, p-, and d-wave scattering. The complexity of the problem is evident if one writes out the explicit forms for the π^--p coefficients in terms of the ten phase shifts.

I feel that if a d-wave phase-shift analysis is desirable it should include all the available data over a wide range of energies, and should be a cooperative effort among various groups interested in the problem. The cost of uncoordinated efforts, in terms of men's time and funds, could be large relative to the amount of information obtained.

Such a program could be undertaken in two steps. Firstly, a small group could analyze the expressions involved in such an analysis to determine what experimental accuracy is necessary--especially for π^--p scattering--to obtain phase shifts of sufficient accuracy to be usefully compared with theory. Secondly, the various groups could contribute toward writing one computer program sufficiently general to process all present data and to make reasonable allowance for future data. Such a general program should be made capable of solving for the "best fit" set of phase shifts as a function of energy by tracking techniques. At least two comprehensive phase-shift analyses including only s- and p-wave scattering have been performed and could form a foundation for such a general d-wave analysis.[32,33]

-93-

ACKNOWLEDGMENTS

-93-

APPENDIX A

This appendix presents the derivation of the data-analysis method. We have discussed the ideas involved in the method and the reasons for its adoption even though it is analytically complicated. The extensive nomenclature required causes some confusion upon initial acquaintance. We must consider three coordiante frames; the π^0-meson rest frame, the π^--p center-of-mass frame, and the laboratory frame. Figure 35 defines the various angles involved. Table XXII defines the necessary symbols. The following nomenclature rules are helpful:

(a) all π^0 quantities in its own rest frame are subscripted zero (i. e., $d\omega_0$),

(b) all π^0 quantities in the c. m. frame have no subscript or superscript (i. e., $d\omega$),

(c) all γ-ray quantities in the c. m. are primed (i. e., $d\omega'$),

(d) all γ-ray quantities in the lab frame are capitalized (i. e., $d\Omega$).

The sole exception is that γ_0 and η_0 denote motion of the c. m. frame in the lab frame.

Table XXII

Symbol	Definition
$\cos^{-1}\alpha$	π^0 angle relative to π^- direction in c. m. frame
$\cos^{-1}x$	γ-ray angle relative to π^0 direction in c. m. frame
$\cos^{-1}y$	γ-ray angle relative to π^- direction in c. m. frame
$\cos^{-1}z$	γ-ray angle relative to π^- direction in lab frame
$d\omega_0$	solid-angle element in π^0 rest frame
$d\omega = d\alpha\, d\zeta'$	solid-angle element into which π^0 goes in c. m. frame
$d\omega' = dx d\zeta'$	solid-angle element into which γ-ray goes in c. m. frame
$d\Omega$	solid-angle element into which γ-ray goes in lab frame
ζ'	azimuth angle associated with $d\omega$ and $d\omega'$ in c.m. frame
γ and η	denote motion of π^0 rest frame in the c. m. frame
γ_0 and η_0	denote motion of c. m. frame in the lab frame

Center-of-mass frame
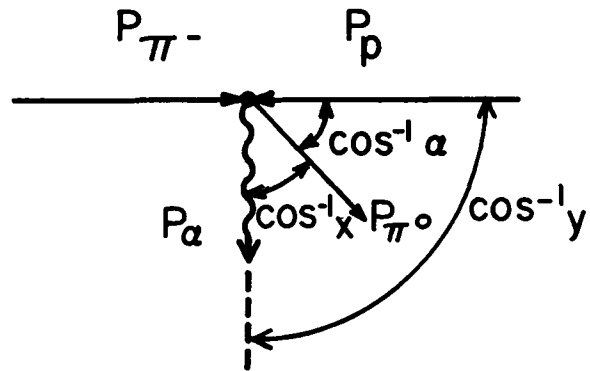
Laboratory frame
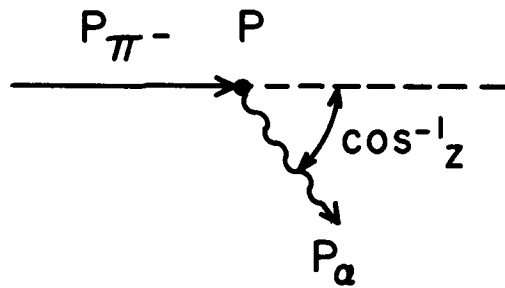
MU – 19814

Fig. 35. Definitions of the angles involved in the derivation of the analysis method.

The π^0 meson's center-of-mass angular distribution may be written

$$\frac{d\sigma_{\pi^0}}{d\omega} = \sum_{\ell=1}^{5} a_\ell P_{\ell-1}(a),$$

(A1),(8)

where index ℓ runs through $\ell = 5$ to include provision for d-wave scattering.

Since the π^0 meson decays isotropically in its own rest frame, the probability for finding a gamma ray in element $d\omega_0$ is

$$2 \times \frac{d\omega_0}{4\pi} = \frac{d\omega_0}{2\pi} .$$

(A2)

The same probability for element $d\omega'$ in the c.m. frame is

$$1/2\pi \left(\frac{d\omega_0}{d\omega'} \right) d\omega',$$

(A3)

and the c.m. differential cross section for gamma-ray production is

$$\frac{d^2\sigma_\gamma(a, x)}{d\omega\, d\omega'} = \left(\frac{d\sigma_{\pi^0}}{d\omega} \right) \frac{1}{2\pi} \left(\frac{d\omega_0}{d\omega'} \right),$$

(A4)

where $\dfrac{d\omega_0}{d\omega'}$ is the Lorentz transformation,[34]

$$\frac{d\omega_0}{d\omega'} = \frac{1}{(\gamma-\eta x)^2} .$$

(A5)

By Eq. (A1) and (A5) we have

$$\frac{d^2\sigma_\gamma(a, x)}{d\omega\, d\omega'} = \frac{1}{2\pi} \frac{1}{(\gamma-\eta x)^2} \sum_{\ell=1}^{5} a_\ell P_{\ell-1}(a),$$

(A6)

expressing the gamma-ray differential cross section in terms of the c.m. angles between π^- and π^0 directions, $\cos^{-1}a$, and between gamma-ray and π^0 directions, $\cos^{-1}x$. Figure 35 shows that this formulation

is undesirable, since we observe neither angle. We do observe the angle between gamma-ray and π^- directions, $\cos^{-1} y$.

The addition theorem for spherical harmonics performs the desired transformation,[35]

$$P_{\ell-1}(\alpha) = \sum_{m=0}^{\ell} A_m P_{\ell-1}^m(x) \cos m\zeta', \tag{A7}$$

$$A_m = (2 - \delta_{m0}) \frac{(\ell-m)!}{(\ell+m)!} P_{\ell-1}^m(y); \tag{A8}$$

δ_{m0} is the Kronecker delta, having unity value for zero m and zero value for nonzero m. The gamma-ray differential cross section becomes

$$\frac{d^2\sigma_\gamma}{d\omega d\omega'} = \frac{1}{2\pi} \frac{1}{(\gamma-\eta x)^2} \sum_{\ell=1}^{5} a_\ell \sum_{m=0}^{\ell} (2-\delta_{m0}) P_{\ell-1}^m(x) P_{\ell-1}^m(y) \cos m\zeta' \tag{A9}$$

We simplify by integrating out the azimuthal dependence of element $d\omega = d x \, d\zeta'$. Owing to the integral

$$\int_0^{2\pi} \cos m\zeta' \, d\zeta' = 0 \text{ for } m \neq 0, \tag{A10}$$
$$= 2\pi \text{ for } m = 0,$$

only the m = 0 term contributes to (A9):

$$\frac{d^2\sigma_\gamma}{dx d\omega} = \sum_{\ell=1}^{5} \frac{a_\ell}{(\gamma-\eta x)^2} P_{\ell-1}(y) P_{\ell-1}(x) . \tag{A11}$$

Integrating out x and transforming to the laboratory frame by

$$\frac{d\omega}{d\Omega} = \frac{1}{(\gamma_0 - \eta_0 z)^2} \tag{A12}$$

yields the gamma-ray differential cross section in the lab frame,

$$\frac{d\sigma_\gamma}{d\Omega} = \frac{1}{(\gamma_0 - \eta_0 z)^2} \sum_{\ell=1}^{5} a_\ell P_{\ell-1}(y) \int_{-1}^{+1} \frac{P_{\ell-1}(x)}{(\gamma - \eta x)^2} \, dx \, . \qquad (A13),(9)$$

The observed net gamma-ray counting rates, $\left(\frac{\gamma}{M}\right)_{net}$, are related to the cross section by defining an "apparent" cross section for gamma-ray production in the c.m. frame,[7]

$$\frac{d\sigma_\gamma}{d\Omega} = \frac{(\gamma/M)_{net}(\gamma_0 - \eta_0 z)^2}{(Nt) \, fG \, \Delta\Omega} , \qquad (A14),(10)$$

where Nt is the average target thickness in protons/cm^2, f is the pion percentage of the beam, G is a geometrical correction factor for finite target and counter size, $\Delta\Omega$ is the subtended solid angle in steradians, and $(\gamma_0 - \eta_0 z)^2$ is the Lorentz transformation factor between the lab and c.m. frames.

Equating (A13) and (A14), we have

$$\frac{(\gamma/M)_{net}(\gamma_0 - \eta_0 z)^2}{Nt \, fG \, \Delta\Omega} = \sum_{\ell=1}^{5} a_\ell P_{\ell-1}(y) \int_{-1}^{+1} \frac{\epsilon(x,z) P_{\ell-1}(x) dx}{(\gamma - \eta x)^2} \, .$$

$$(A15),(11)$$

The explicit energy dependence of the gamma-ray detection efficiency is thus incorporated into the analysis. This treatment is exact except for the slight dependence of $G \Delta\Omega$ on x. The dependence has been accounted for by using a properly averaged value for $G\Delta\Omega$.

It is convenient to define

$$\bar{\epsilon}_\ell(z) \equiv \frac{1}{k_\ell} \int_{-1}^{+1} \frac{\epsilon(x,z)P_{\ell-1}(x)dx}{(\gamma-\eta x)^2} \, , \tag{A16}, (12)$$

$$k_\ell \equiv \int_{-1}^{+1} \frac{P_{\ell-1}(x)dx}{(\gamma-\eta x)^2} \, ,$$

$$Y(z) = \frac{(\gamma/M)_{net}(\gamma_0 - \eta_0 z)^2}{(Nt) f G \Delta\Omega} \, .$$

Equation (A15) becomes

$$Y(z) = \sum_{\ell=1}^{5} a_\ell X_\ell(z) \, , \tag{A17}, (13)$$

where

$$X_\ell(z) = P_{\ell-1}(y) \, \bar{\epsilon}(z) \, k_\ell \, , \tag{18}, (14)$$

We obtain for each lab observing angle one linear equation, (A17), in terms of the desired coefficients a_ℓ. (A least-squares solution for the a_ℓ by IBM 650 computer is described in Section IV.)

We show lastly that the gamma-ray counter detection efficiency is a function only of x and z. Angles in two coordinate frames moving relativistically with respect to each other are related by the aberration formula,

$$y = \left(\frac{\gamma_0 z - \eta_0}{\gamma_0 - \eta_0 z}\right), \tag{A19}, (15)$$

where y is cosine of the angle in the moving frame (c.m. frame), z is cosine of the lab observing angle, and γ_0 and η_0 denote the c.m. frame velocity observed at $\cos^{-1} z$ (lab) is obtained by Lorentz transformation

of the fourth component of the photon's 4-momentum vector from

(a) the π^0 rest frame to the c.m.frame, and then

(b) from the c.m. frame to the lab frame.[34]

The result is

$$K = K_0 \frac{(\gamma_0 + \eta_0 y)}{(\gamma - \eta x)} , \tag{A20}$$

where K_0 is one-half the π^0 rest energy, γ and η denote motion factors of the π^0 rest frame in the c.m. frame, and K is the observed photon energy. The forms of Eqs. (A19) and (A20) show that the detector efficiency, $\epsilon(K)$, is a function of only x and z.

APPENDIX B

Expressions necessary to obtain the gamma-ray counter efficiency from experimental measurements are derived as follows:

The number of gamma-ray telescope counts per μcoulomb may be written

$$Y_i = \int_{K_{th}}^{K_{max_i}} \epsilon(K) N_i(K)\, dK, \tag{B1}$$

where $\epsilon(K)$ is the desired counter efficiency, in counts per photon; $N_i(K)$ is the bremsstrahlung spectrum for peak photon energy K_{max_i}, in photons per Mev; and K_{th} is the threshold energy of the counter, in Mev. The counter telescope is insensitive to incident photons of energy less than K_{th}.

From a preliminary calibration experiment we learned that the efficiency was closely approximated by the function

$$\epsilon(K) = a \ln \left(\frac{K}{K_{th}} \right), \tag{B2},(19)$$

where K is the incident photon energy in Mev, and the parameter to be determined is a in counts/photon. Provision was made in our analysis for consideration of a more complicated efficiency function,

$$\epsilon(K) = a \ln \left(\frac{K}{K_{th}} \right) - (K - m)^n, \tag{B3}$$

where m is an energy parameter (in Mev) denoting that the efficiency departs from a $\ln K$ dependence and n is an appropriate dimensionless exponent. Our analysis demonstrated that within the experimental accuracy Eq. (B2) was a sufficiently good approximation.

Let us define

$$\ell \equiv \ln K_{th}, \tag{B4}$$

and the constant, a_i, having dimensions of photons/μcoulomb, by

$$a_i B_i(K) \equiv K N_i(K), \tag{B5}$$

where $B_i(K)$ are the Schiff bremsstrahlung spectra.[20]

Equation (B1) becomes

$$\gamma_i = \alpha\, a_i \int_{K_{th}}^{K_{max_i}} (\ln K - \ell)\, \frac{B_i(K)}{K}\, dK. \tag{B6}$$

It is convenient to define the integrals

$$A_i \equiv \int_{K_{th}}^{K_{max_i}} \ln K\, \frac{B_i(K)}{K}\, dk,$$

$$B'_i \equiv \int_0^{K_{max_i}} B_i(K)\, dK, \tag{B7}$$

$$C_i \equiv \int_{K_{th}}^{K_{max_i}} \frac{B_i(K)}{K}\, dK.$$

A_i and C_i are dimensionless; B_i is in Mev.

The parameter α is given by

$$\alpha = a_i\, \frac{\left[A_i - \ell\, C_i\right]}{\gamma_i}. \tag{B8),(20}$$

One such equation is obtained from measurements at each peak energy K_{max_i}.

The constant a_i is obtained by means of the definition of effective quanta, Q:[36]

$$N_i = Q_i K_{max_i} = \int_0^{K_{max_i}} K \, N_i(K) \, dk. \tag{B9}$$

By (B5) we have

$$N_i = a_i \int_0^{K_{max_i}} B_i(K) \, dK, \tag{B10}$$

and, by (B7)

$$a_i = \frac{N_i}{B_i} \, , \tag{B11},(24)}$$

where N_i is in Mev/μcoulomb and B_i is in Mev.

References

1. S. M. Korenchenko and V. G. Zinov, International Conference on Mesons and Recently Discovered Particles, Padua-Venice, Sept. 1957.

2. V. G. Zinov and S. M. Korenchenko, Zhur. Eksptl. i Teoret. Fiz. 36, 618-619 (February, 1959).

3. J. Tinlot and A. Roberts, Phys. Rev. 95, 137 (1954).

4. Bodansky, Sachs, and Steinberger, Phys. Rev. 93, 1367 (1954).

5. Anderson, Fermi, Martin, and Nagle, Phys. Rev. 91, 155 (1953).

6. Ashkin, Blaser, Feiner, and Stern, Phys. Rev. 101, 1149 (1956).

7. H. L. Anderson and M. Glicksman, Phys. Rev. 100, 268 (1955).

8. Fermi, Glicksman, Martin, and Nagle, Phys. Rev. 92, 161 (1953).

9. M. Glicksman, Phys. Rev. 94, 1335 (1954).

10. M. Glicksman, Phys. Rev. 95, 1045 (1954).

11. Ashkin, Blaser, Feiner, and Stern, Phys. Rev. 105, 724 (1957).

12. Garwin, Kernan, Kim, and York, Phys. Rev. 115, 1295 (1959).

13. Kernan, York, and Garwin, Bull. Am. Phys. Soc. Ser. II, 4, 401 (1959).

14. Frank Evans, in Lawrence Radiation Laboratory Counting Handbook, UCRL-3307 (Rev), Jan. 1959. Sec. CC 3-7

15. David F. Swift and Victor Perez-Mendez, Millimicrosecond Discriminator, UCRL-8569, Dec. 1958.

16. Duane D. Newhart, Victor Perez-Mendez, and William L. Pope, Liquid-Hydrogen Target, UCRL-8857, Aug. 1959.

17. Walton A. Perkins, III, Positive-Pion Production by Negative Pions, UCRL-8778, June 1959.

18. W. E. Deming, Statistical Adjustment of Data (John Wiley and Sons, New York 1943) Chapters IV and VIII.

19. Corson, DeWire, McDaniel, and Wilson, The Cornell 300-Mev Synchrotron, Floyd Newman Lab of Nuclear Studies, NP-4972 (July 1953).

20. L. I. Schiff, Phys. Rev. 83, 252 (1951). Calculations by Larry Higgins (UCRL), private communication.

21. F. J. Loeffler, T. R. Palfrey, and G. W. Tautfest, The Energy Dependence of the Cornell Thick-Walled Ionization Chamber (submitted to Nuclear Instruments).

22. Lindenfeld, Sachs, and Steinberger, Phys. Rev. 89, 531 (1953).

23. H. A. Bethe and F. de Hoffman, Mesons and Fields, Vol. II (Row-Peterson and Company, Evanston, Illinois 1955) Sec. 36.

24. G. Neugebauer, W. D. Wales, and R. L. Walker, Phys. Rev. Letters 2, 429 (1959).

25. F. P. Dixon and R. L. Walker, Phys. Rev. Letters 1, 458 (1958).

26. R. D. Evans, The Atomic Nucleus (McGraw-Hill Book Co., New York 1955), Chapter 27.

27. Peter Cziffra and Michael J. Moravscik, A Practical Guide to the Method of Least Squares, UCRL-8523, Oct. 1958.

28. Peter Cziffra, (Lawrence Radiation Laboratory), private communication.

29. L. K. Goodwin, R. W. Kenney, and Victor Perez-Mendez, Phys. Rev. Letters 3, 522 (1959).

30. Lester K. Goodwin, (Lawrence Radiation Laboratory), private communication.

31. Foote, Chamberlain, Rogers, Steiner, Wiegand, and Ypsilantis, Phase Shifts in π^+-p Scattering at 310 Mev, UCRL-8981, Nov. 1959.

32. de Hoffman, Metropolis, Alei, and Bethe, Phys. Rev. 95, 1586 (1954).

33. H. Y. Chiu and E. L. Lomon, Annals of Physics 6, 50 (1959).

34. L. Landau and E. Lifshitz, The Classical Theory of Fields (Addison-Wesley, Cambridge, Mass. 1951) p. 121.

35. W. R. Smythe, Static and Dynamic Electricity (McGraw-Hill Book Co., New York 1950), Section 5.24.

36. P. Morrison, in Experimental Nuclear Physics, E. Segrè, Ed. Vol. II (John Wiley and Sons, New York 1953).